Chemical Engineering Journal 437 (2022) 135317

Contents lists available at ScienceDirect

Chemical Engineering Journal

journal homepage: www.elsevier.com/locate/cej

A comprehensive multi-scale model for bipolar membrane electrodialysis (BMED)

Andrea Culcasi, Luigi Gurreri, Andrea Cipollina, Alessandro Tamburini *, Giorgio Micale

Dipartimento di Ingegneria, Università degli Studi di Palermo – Viale delle Scienze ed. 6, 90128 Palermo, Italy

ARTICLE INFO

Keywords:
Electro-membrane process
Ion-exchange membrane
Bipolar membrane
Process simulator
Chemicals production, electrodialysis

ABSTRACT

Bipolar membrane electrodialysis (BMED) is a technology combining solute and solvent dissociation to produce chemicals. In the recent decades, it has been typically studied for the production of valuable acid and base solutions from salt streams. Although many works have been devoted to the experimental investigation of BMED, only a few efforts have focused on its mathematical modelling. In the present work, a comprehensive process model based on a multi-scale approach with distributed parameters is presented for the first time. Five models related to four different dimensional scales were fully integrated to form a comprehensive tool. The integrated model was developed by using the process simulator gPROMS Model builder and was based on a semi-empirical approach combining high prediction accuracy and low computational demand. Once validated through a wide range of experimental data, the model capability was shown by carrying out a broad sensitivity analysis assessing the performance of the BMED technology for industrial-scale applications. Results showed how the performance of a BMED unit changes with both varying process conditions and the installed membrane area. Particularly, the non-ideal phenomena that reduce the produced NaOH concentration and increase the energy consumption were thoroughly investigated. Finally, this study demonstrated that a Levelized Cost Of Caustic Soda of about 280 € ton^{-1}_{NaOH} can be obtained, thus making this technology a possible candidate for the industrial production of caustic soda from brines in the future.

1. Introduction

Bipolar membrane electrodialysis (BMED) is an efficient method for the production of acid and base solutions [1]: its eco-friendly qualities have attracted increasing attention from both academia and industry [2,3]. A BMED device is characterized by the presence of bipolar membranes (BPMs) that allow the water to dissociate, separating proton and hydroxide ions, thus producing acid and base solutions. A scheme of the BMED process is depicted in Fig. 1. The repetitive unit of a BMED stack is named cell (or triplet) and it is composed of three channels (i.e., saline, basic and acid channel) and three different ion-exchange membranes, IEMs (i.e., an anion-exchange membrane AEM, a cation-exchange membrane CEM and a BPM).

In principle, fresh water enters the acid and base channels while salt water enters the salt channel (inlet streams in Fig. 1). In the interlayer of the bipolar membrane, thanks to the applied voltage, water dissociation occurs thereby producing proton ions and hydroxide ions driven towards opposite directions by the electric field (Fig. 1). The salt ions in the salt channel are also forced to move towards opposite directions depending on their charge. As a result, the production of the acid and base is achieved.

BMED is a very versatile technology as it may be used for synthesis processes and, very recently, it has been proposed in its reverse mode, namely the Bipolar Membrane Reverse ElectroDialysis (BMRED) [4], which allows the production of energy from the acid and base neutralization. The BMED-BMRED combination has recently been studied for energy storage [5].

1.1. Industrial applications of the BMED process

BMED has been studied for the production of several organic and inorganic acids, as well as alkaline solutions. BMED may be used in the food industry [6], chemical and biochemical productions [7], and wastewater treatment [3,8]. For example, BMED can produce high value citric acid [6], which can be used in food and pharmaceuticals [6,9]. Formic acid is also a potential output of BMED [10], and this has been shown to be an efficient process despite the well-known acid diffusion phenomenon. Unlike other methods, BMED has the advantage of the concurrent production of an alkaline solution (e.g., sodium hydroxide),

* Corresponding author.
E-mail address: alessandro.tamburini@unipa.it (A. Tamburini).

https://doi.org/10.1016/j.cej.2022.135317
Received 27 October 2021; Received in revised form 9 February 2022; Accepted 15 February 2022
Available online 18 February 2022

Nomenclature

Symbols

a (mol m^{-3}) ion activity
A (m^{-2}) membrane area
b (m) spacer width
C (mol m^{-3}) molar concentration
CapitalCost (€) initial total capital investment
CostElectricity (€ y^{-1}) annual cost of the electricity consumed by the BMED
d (m) generic thickness
D (m^2 s^{-1}) diffusion coefficient
E (V) triplet electromotive force corrected for concentration polarization
F (C mol^{-1}) Faraday constant
i (A m^{-2}) current density
I (A) current intensity
I_{loss} (-) % parasitic loss of current
J (mol m^{-2} s^{-1}) effective molar flux
L (m) spacer length
L_p (ml m^{-2}h^{-1} bar) osmotic permeability
LCoNaOH (€ ton$^{-1}_{NaOH}$) Levelized Cost of NaOH
M (g mol^{-1}) molar mass
Mass (ton) annual mass of caustic soda produced
N (-) number of triplets
O&M (€ y^{-1}) annual cost of operation
PPD (W m^{-2}) pumping power density
Q (m^3 s^{-1}) volume flow rate
r (-) discount rate
R (Ω) generic electric resistance
R_g (J mol^{-1} k^{-1}) gas constant
SEC_m (kWh kg$^{-1}_{NaOH}$) Specific Energy Consumption per kg of NaOH
$SEC_{m,net}$ (kWh kg$^{-1}_{NaOH}$) Net Specific Energy Consumption per kg of NaOH
SEC_v (kWh m^{-3}) Specific Energy Consumption per m^3 of alkaline solution
SP (kg m^{-2} y^{-1}) Specific productivity
t (s) time
t_i (-) ion transport number
t_i^* (-) apparent ion transport number
T (K) temperature
T_R (s) residence time
u (cm s^{-1}) mean channel flow velocity
U (V) potential difference applied to all the triplets
U_{ext} (V) overall applied potential
V (m^3) generic volume
ΔV (V) generic voltage difference
X (mol m^{-3}) fixed charge density in the membrane
y (y) year
z (-) ion charge

Greek letters

η_{c,OH^-} (-) OH^- current efficiency
τ_{NaOH} (-) NaOH yield

Subscripts/superscripts

a	acid
av	average over the triplet
AEL	anionic exchange layer
b	base
bl	blank
BPL	bipolar membrane layer
c	collector
cell	repeating unit (triplet)
co	co-ion
ct	counter-ion
CEL	cationic exchange layer
d	distributor
diff	diffusive
ext	external
i	ion species
IEM	ion exchange membrane
in	inlet
int	interface
k	generic cell-triplet in the stack
left	left side
lim	limiting
m	membrane
man	manifold
mig	migrative
out	outlet
right	right side
s	salt
sol	solution
tr	transition region (interlayer)
x	lateral (i.e., up or down)
y	year

Acronyms/abbreviations

AEL	Anion-Exchange Layer
AEM	Anion-Exchange Membrane
BMED	Bipolar Membrane ElectroDialysis
BMRED	Bipolar Membrane Reverse ElectroDialysis
BPM	Bipolar Membrane
CEL	Cation-Exchange Layer
CEM	Cation-Exchange Membrane
CFD	Computational Fluid Dynamics
DSA	Dimensionally Stable Anode
ECTFE	Ethylene ChloroTriFluoroEthylene
ERS	Electrode Rinse Solution
FCD	Fixed Charge Density
IEC	Ion Exchange Capacity
LCoNaOH	Levelized Cost Of Caustic Soda
NET	Non-Equilibrium Thermodynamic
N-P	Nernst-Planck
PVC	Polyvinyl chloride
SD	Swelling Degree

which can be sold or re-circulated into other processes [11]. Therefore, BMED may be smartly employed in those processes that need pH-control, e.g. whey acid neutralization [12–16]. Furthermore, BMED can also be utilised to recover other high value resources, including lithium and boron, with high separation efficiency [17–19].

Another possibility is the use of BMED for the recovery of sodium chloride streams [20], or in the desalination industry [21–23], by converting the saline input into hydrochloric acid and sodium hydroxide solutions. HCl can be recirculated into the pre-treatment steps of the plant [22], and both acid and base can be used for membrane cleaning. Finally, the desalination of the brine allows it to be recovered, achieving a circular economy with zero liquid discharge [24,25]. The energy consumption of BMED depends on the operating conditions, with ranges of 2.3–17 kWh kg^{-1} of NaOH produced at concentrations ranging between 0.18 M and 2.4 M [22], or 1.3–18 kWh kg^{-1} of HCl produced at concentrations ranging between 0.45 M and 1.99 M [22,23]. The

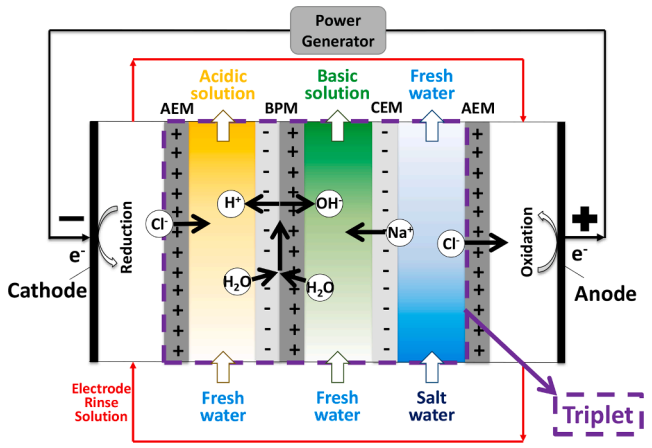

Fig. 1. Scheme of a Bipolar Membrane ElectroDialysis (BMED) unit. The purple block indicates the triplet (i.e., the repetitive unit of the stack).

common range of current densities is 250–1,000 A m^{-2} [26], but it can be up to 2,000 A m^{-2} with certain bipolar membrane (BPM) characteristics [27]. However, current densities as high as 500 A m^{-2} are a good compromise between reducing the membrane area [10] (and, thus, the capital cost [28]), and limiting the ohmic losses.

1.2. Modelling of the Bipolar membrane electrodialysis: state of the art

Although BMED has been widely investigated by experimental works, further studies are required to develop effective simulation tools that are able to predict the functioning, to optimize the systems, and eventually to drive the scale-up to the industrial level [29]. Table 1 gives an overview of different BMED modelling approaches, highlighting some of their relevant characteristics.

The models presented so far are simplified tools with lumped parameters, based at least on three empirical parameters [30], and with six-eight constants on average [31]. Mass balances are commonly included to predict the outlet concentrations from the unit [31,32]. However, only one model takes into account local mass balances [33] (distributed parameters).

Regarding the *trans*-membrane flux calculations, the Nernst-Planck (N-P) approach is generally used [26,33–36], while the membrane fluxes are described by the non-equilibrium thermodynamics (NET) in some cases [37]. The concentrations at the membrane side of the solution-membrane interface are evaluated by applying the Donnan equilibrium equations [33,36,38]. The interface concentration at the solution side is different from the bulk concentration because of the effects of the boundary layer (concentration polarization). Although generally not considered for the sake of simplicity, the boundary layer may have a considerable impact, especially in the salt compartment [38]. Among others, this phenomenon is related to the diffusion-limited current at the monopolar membranes in the salt channel [37,39] (this should not be confused with the first bipolar limiting current [27]). Indeed, the diffusion-limited current is theoretically obtained when the electrolyte concentrations at the interface become zero [40].

Aside from very few cases ([33,36,38]) all the models presented in Table 1 do not take into account the ion concentrations in the membrane phase, as well as the Donnan equilibrium at the solution-membrane interfaces and the effect of the diffusion potential on the performance.

Modelling tools for BMED systems are often limited to the computation of the migrative flux, while the ion diffusion is taken into account only in a few cases [31,37,41]. However, the diffusive flux is important for a more complete prediction of the proton leakage through the AEMs [32,41], as well as, in general, for predicting the leakage of all co-ions. Moreover, the water flux, due to the osmotic and electro-osmotic contributions, has been included only in a few models [32,37].

Regarding the voltage-current behavior, the electromotive force has

Table 1
List of the main characteristics of BMED models presented in the literature.

Reference	Domain		Mass balances	Membrane flux approach		Non-ideal phenomena					Hydraulic calculations
	lumped	distributed		[1]N-P	[2]NET	Diffusion		Co-ion migration	Shunt currents	Concentration Polarization	
						water	solutes				
Koter and Warszawski [31], 2006	✓	X	✓	X	X	X	✓	✓	X	X	X
Gineste et al. [32], 1996	✓	X	✓	X	X	✓	✓	✓	X	X	X
Mier et al. [26], 2008	✓	X	X	✓	X	X	✓	✓	X	✓	X
Vera et al. [35], 2009	✓	X	X	X	X	X	X	✓	X	X	X
Koter [38], 2007	✓	X	X	✓	X	X	✓	✓	X	✓	X
Roux-de Balmann et al. [30], 2002	✓	X	X	X	X	X	X	X	X	X	X
Shi et al. [41], 2018	✓	X	✓	X	X	X	✓	✓	X	X	X
Wang et al. [36], 2011	✓	X	✓	✓	X	X	✓	✓	X	✓	X
Jiang et al. [34], 2019	✓	X	X	✓	X	X	✓	X	X	X	X
Melnikov et al. [37], 2020	✓	X	✓	X	✓	✓	✓	X	X	X	X
Ortega et al. [33], 2022	X	✓	✓	✓	X	X	✓	✓	X	✓	X
Present model	X	✓	✓	✓	X	✓	✓	✓	✓	✓	✓

[1] Nernst-Planck.
[2] Non-Equilibrium Thermodynamics.

been calculated by using the Nernst equation [35]. The electric potential applied to the electrodes is commonly calculated by considering an ideal equivalent electrical circuit, in which the electrical current circulating in the external circuit is identical to that circulating in the BMED stack (cell by cell), thus ignoring the effect of the so-called parasitic currents (also known as shunt currents). However, they are a source of irreversibility, which dramatically affects the BMED performance [42]. This phenomenon arises in a BMED module because the channels of the same type are arranged hydraulically in a parallel configuration. This leads to the existence of salt-bridges, which act as secondary pathways through the manifolds, i.e. the distributors and collectors, especially in the case of highly conductive solutions. With a fixed target acid/base concentration, and for any value of internal average current, parasitic currents cause an increase in the external current applied by the power supplier. Consequently, the BMED consumes higher amounts of energy.

Although parasitic currents have been characterized for conventional electrodialysis and reverse electrodialysis [42–44], they have been poorly studied so far for BMED processes. The effect of shunt currents was found to be greater when the internal resistance increases [45]. Therefore, the use of low-resistance membranes, as well as of thin spacers, may minimize these effects [46].

Although the BMED models presented in the literature do not account for parasitic currents, their predictions agree fairly well with experimental data. This is because the model validation has been performed by using BMED stacks with a low number of triplets, within the range 1–10, which leads to low or even negligible effects of shunt currents [42]. Conversely, parasitic currents and their effects can be significant in stacks with more triplets, which are of practical interest for pilot and industrial applications. Therefore, an effective modelling tool able to predict the behavior of a BMED unit by varying the main design stack features should include the simulation of shunt currents.

Finally, the prediction of the BMED performance should incorporate the calculation of the pumping power consumption in order to evaluate the overall energy requirement. To this purpose, a set of hydraulic equations could be beneficial to estimate pressure losses throughout the stack, as well as the flow rate distribution channel by channel.

All the aspects discussed so far may play an important role and deserve proper attention: all of the involved phenomena should be taken into full account to build a comprehensive tool with high prediction capabilities. The mathematical models already developed in the literature are not inclusive to such an extent, as they focus only on specific aspects. Therefore, these models have not a general validity but are strictly reliable under certain design and operating conditions only. Conversely, a comprehensive mathematical model is needed to thoroughly assess BMED systems' performance, especially at a large scale where some detrimental phenomena may be crucial and become the actual bottleneck for the technology's spread.

This work aims at developing a simulation tool able to simulate simultaneously all the main phenomena occurring in BMED units and, thus, to provide reliable predictions of the process performance under very different conditions and scales. The present mathematical model was developed with distributed parameters and with a multi-scale approach by also including the simulation of parasitic currents. It was implemented to simulate the BMED process for the production of HCl and NaOH solutions. Experimental data across a wide range of operating conditions were collected to validate the model. A sensitivity analysis and a preliminary techno-economic assessment were performed to show the model capabilities and the potential application of the BMED process.

2. Experimental

A lab-scale test-rig was employed to validate the model. The experimental setup was a FT-ED-100 module purchased from Fumatech BWT GmbH (Germany) and assembled with fumasep® FAB, FKB and FBM anion-exchange, cation-exchange, and bipolar membranes, respectively.

The BMED unit was assembled with a number of cells (or triplets) ranging from 5 to 38. The membrane active area was a 100 cm^2 square, and the membranes were separated by woven spacers made of PVC/ECTFE and 475 μm thick. The solutions enter/exit respectively the channels via 3 inlet/outlet holes of 8 mm diameter. DSA were used as electrodes. The blank resistance (due to electrode chambers along with the end-membrane, the electromotive force of the anode/cathode reactions and the relevant over-voltages) was 72 Ω cm^2 when using an aqueous electrode rinse solution (ERS) made up of 0.5 M in $FeCl_2/FeCl_3$ (99% ChemSolute) and 0.6 M in HCl. The concentration of $FeCl_2/FeCl_3$ and a mean flow velocity of 3 cm s^{-1} in the electrode chambers were purposely chosen (as a result of preliminary mass balances calculation) in order to avoid any mass transfer kinetic control at the electrodes. HCl was added in the ERS to prevent the precipitation of oxy-hydroxide compounds. The acid, base and salt feed solutions were prepared with demineralized water, HCl (37% Merck), NaOH (98–100% Honeywell Fluka) and NaCl (NaCl 99.7% ChemSolute). Acid and base solutions were fed with a co-current layout, while the salt solution was fed with a cross-flow arrangement. All the solutions were forced to flow through the unit by BT601S volumetric pumps (Lead Fluid Technology, CO LTD, China). The experiments were carried out either in steady-state once-through mode with 10–38 triplets or in dynamic closed-loop mode (recirculation of the solutions into the tanks) with 5 triplets, as schematically depicted in Fig. 2. In the former case, the flow velocity was 1 cm s^{-1}, while in the latter case it was 0.2 cm s^{-1}. The experiments were conducted at room temperature. A constant electric current was applied in each experiment (galvanostatic mode) by using a BK Precision 1902 DC Power Supply. To check the repeatability of the experiments, a test was conducted at the same operating conditions at least twice. Both titration and chromatography (Metrohm 882 Compact Ion Chromatography, samples diluted with Milli-Q water) analyses were performed for evaluating the ion concentrations in the inlet and outlet solution samples.

In once-through mode, the unit operated continuously until a steady-state condition was reached (stable voltage). Steady-state voltage-current curves were obtained. These may be grouped into two sets based on the presence or not of 0.25 M NaCl in the acid and base compartments. The different operating conditions tested are listed in Table 2.

Regarding the closed-loop tests, these were carried out until one out of three possible conditions was met: (i) NaCl concentration approaching zero in the salt compartments, detected by a sharp increase in external voltage; (ii) target concentration of NaOH of 1 M (typical of BMED testing) being attained; (iii) a constant value of NaOH concentration being achieved. The experiments were conducted with the operating conditions and starting concentrations listed in Table 3.

3. Description of the multi-scale model

The most common BMED configuration with three-chamber repetitive units (BPM-CEM-AEM membranes with acid, salt and base solutions) was simulated. Four different scales were simulated with a multi-scale model composed of a total of five different models developed with a distributed parameters approach. Each channel in the stack had 30 domain intervals along the main flow direction, which were more than sufficient to avoid grid-dependence problems, thus ensuring a good numerical accuracy. The model was discretized only in the axial direction, with no discretization in the cross-stream direction (i.e., perpendicular to the membrane). Cross-stream concentration gradients, however, were estimated for each element of the axial discretization, both with reference to the channels and the membranes. Concerning the channels, for each element of the discretization domain, both the bulk and interface concentrations were calculated using suitable equations accounting for polarization phenomena [47]; regarding the membranes, for each element of the discretization domain, the membrane side concentration was calculated by applying the Donnan equilibrium to both membrane sides and assuming a linear concentration profile inside the

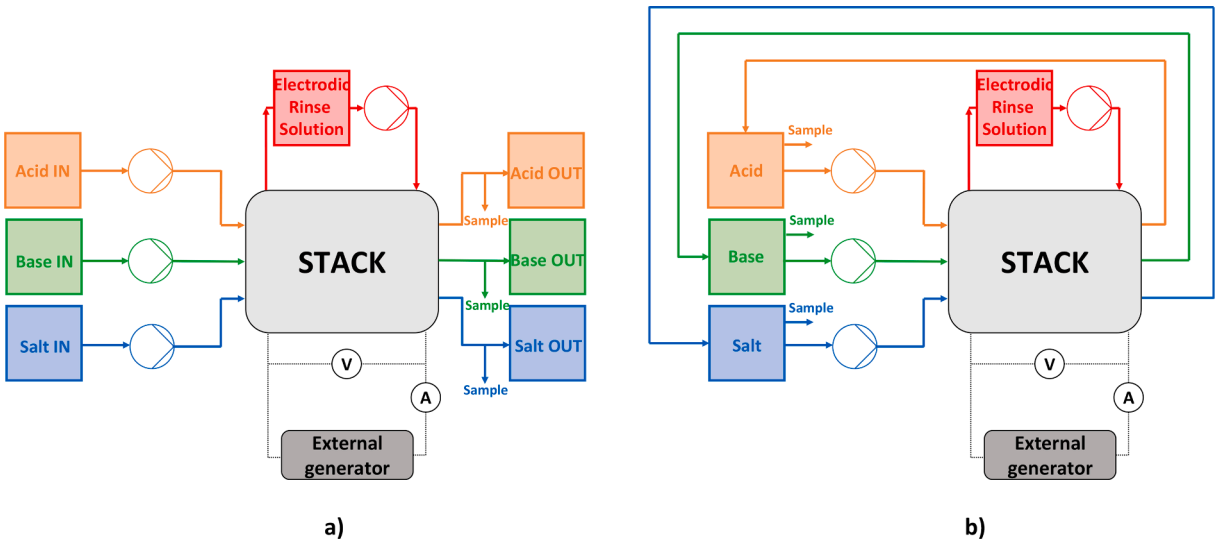

Fig. 2. Schemes of the adopted experimental configurations: (a) once-through (steady state) and (b) closed-loop (transient).

Table 2
Operating conditions and inlet concentrations for the steady-state once through experiments. Areal blank resistance: 72 Ω cm^2.

		without background salt	with background salt
N° triplets (N)	–	20–38	10–30
HCl concentration in the acid solution ($C_{a,HCl,in}$)	mol m^{-3}	200	200
NaCl concentration in the acid solution ($C_{a,NaCl,in}$)	mol m^{-3}	0	250
NaOH concentration in the base solution ($C_{b,NaOH,in}$)	mol m^{-3}	200	200
NaCl concentration in the base solution ($C_{b,NaCl,in}$)	mol m^{-3}	0	250
NaCl concentration in the salt solution ($C_{s,NaCl,in}$)	mol m^{-3}	250	250
Mean flow velocity ($u_{ch,sol}$)	cm s^{-1}	1.0	1.0
Applied current density (i_{ext})	A m^{-2}	20–250	20–250

Table 3
Operating conditions and starting concentrations for the closed-loop experiments. Areal blank resistance: 72 Ω cm^2.

N° triplets (N)	-	5
HCl concentration in the acid solution ($C_{a,HCl,in}$)	mol m^{-3}	100
Acid solution volume ($V_{a,in}$)	l	0.6
NaOH concentration in the base solution ($C_{b,NaOH,in}$)	mol m^{-3}	100
Base solution volume ($V_{b,in}$)	l	0.6
NaCl concentration in the salt solution ($C_{s,NaCl,in}$)	mol m^{-3}	1,000
Salt solution volume ($V_{s,in}$)	l	0.6
Mean flow velocity ($u_{ch,sol}$)	cm s^{-1}	0.2
Applied current density (i_{ext})	A m^{-2}	200

membrane.

Except for the bipolar membrane model, the other models were developed in a previous work [47]. Fig. 3 depicts the structure of the multi-scale model.

From the lowest scale of the channels and bipolar membrane up to the stack level (included), all the models simulate the steady-state operation. The highest scale includes the simulation of the external hydraulic circuit, which takes into account the dynamic behaviour of BMED with closed-loop configurations. All the models are integrated in the gPROMS Model Builder® platform, which is an equation-oriented software particularly suitable to build multi-scale model tools with a hierarchical structure.

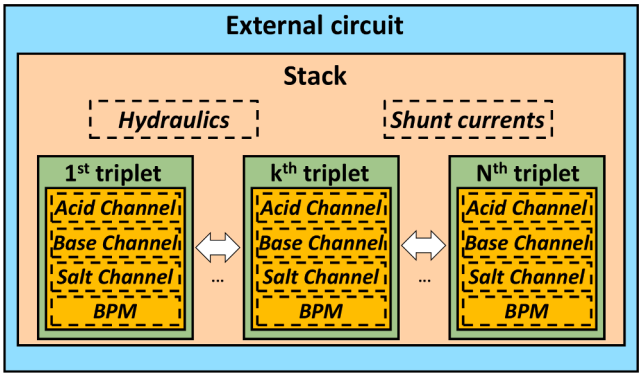

Fig. 3. Scheme of the multi-scale model: levels or scales (frames with continuous lines) and sub-models (frames with dashed lines, text in italics).

3.1. Lowest scale

The lowest scale consists of two models: the channel model and the bipolar membrane model. The former calculates the chemical-physical properties of the electrolyte solutions, while the latter estimates the limiting current density of NaCl and the fluxes through the bipolar membrane layers.

3.1.1. Channel model

The model of the channels calculates the mass density using the approach of Laliberté and Cooper [48], the activity coefficients using the multi-electrolyte Pitzer virial equations [49,50], and the conductivity, viscosity and ionic diffusivities by means of the database of the OLI studio® software. It also derives the values of Sherwood numbers and Fanning friction factors in the spacer-filled channels from correlations provided by Computational Fluid Dynamics (CFD) simulations [47].

3.1.2. Bipolar membrane model

The bipolar membrane is composed of two different layers, a cation-exchange layer (CEL) and an anion-exchange layer (AEL). The BPM model is devoted to the estimation of the salt limiting current, and ion fluxes through each of the two layers. Through the CEL, the migrative flux is calculated for H^+, Na^+ and Cl^- ions, while the diffusive flux is assessed only for the latter two. On the other hand, through the AEL, the

migrative flux is attributed to OH^-, Na^+ and Cl^-, while the diffusive flux is calculated for Na^+ and Cl^- only. The calculation of the migrative fluxes involves the salt limiting current density. It is the maximum current before the interlayer becomes depleted of salt ions and water dissociation begins. By following Strathmann's approach [27], the limiting current is assessed by computing a mass balance in the interlayer of the BPM (see Fig. 4) for the sodium ion. Indeed, these balances calculated using sodium ions are sufficient for evaluating the limiting current density.

The mass balance in the BPM interlayer is calculated as:

$$V_{tr}\frac{dC_{Na,tr}}{dt} = A\left(J_{mig,Na,AEL} + J_{mig,Na,CEL} + J_{diff,Na,AEL} + J_{diff,Na,CEL}\right) \quad (1)$$

where V_{tr} is the BPM transition region (interlayer) volume, $C_{Na,tr}$ is the sodium ion concentration in the interlayer, A is the membrane area, $J_{mig,Na,AEL}$ and $J_{mig,Na,CEL}$ are the migrative fluxes of sodium ions in the AEL and CEL respectively, $J_{diff,Na,AEL}$ and $J_{diff,Na,CEL}$ are the diffusive fluxes of sodium ions in the AEL and CEL, respectively. In fact, following the Strathmann's assumption, the bipolar membrane is modelled as symmetrical. Migrative and diffusive fluxes are calculated as follows:

$$J_{mig,Na,AEL} = \frac{t_{Na,AEL}i_{lim}}{z_{Na}F} \quad (2)$$

$$J_{mig,Na,CEL} = -\frac{t_{Na,CEL}i_{lim}}{z_{Na}F} \quad (3)$$

$$J_{diff,Na,AEL} = D_{NaCl}\frac{C_{Na,AEL,ch} - C_{Na,AEL,tr}}{d_{AEL}} \quad (4)$$

$$J_{diff,Na,CEL} = D_{NaCl}\frac{C_{Na,CEL,ch} - C_{Na,CEL,tr}}{d_{CEL}} \quad (5)$$

in which i_{lim} is the limiting current density, $t_{Na,AEL}$ and $t_{Na,CEL}$ are the sodium ion transport numbers in the two layers of the BPM, z_{Na} is the sodium ion valence, F is the Faraday constant, D_{NaCl} is the salt diffusion coefficient (i.e., 2×10^{-11} m^2 s^{-1}), $C_{Na,AEL,ch}$ and $C_{Na,CEL,ch}$ are the sodium ion concentrations in the AEL and CEL layers, respectively, at the channel side, $C_{Na,AEL,tr}$ and $C_{Na,CEL,tr}$ are the sodium ion concentration in the AEL and CEL layers, respectively, at the transition region, and d_{AEL} and d_{CEL} are thicknesses of the AEL and CEL, respectively.

It is assumed that the ion transport numbers related to the limiting current density are 99% for the counter-ion and 1% for the co-ion [27]. Therefore, the sodium and chloride ion transport numbers are related to i_{lim} as:

$$t_{Na,AEL} = 0.01 \bullet \mathrm{abs}\left(\frac{i_{lim}}{i}\right) \quad (6)$$

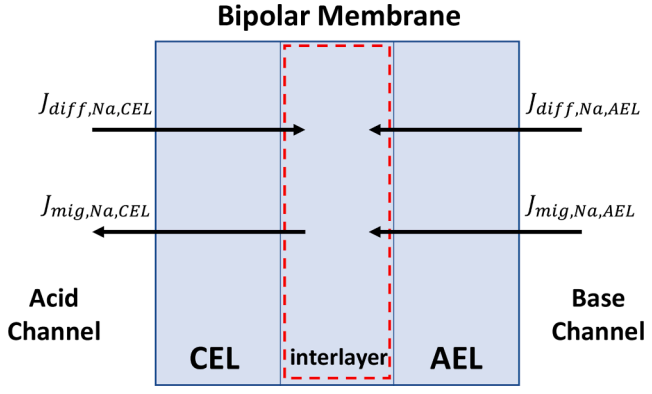

Fig. 4. Ion fluxes across the cation- and anion-exchange layers of the bipolar membrane.

$$t_{Cl,AEL} = 0.99 \bullet \mathrm{abs}\left(\frac{i_{lim}}{i}\right) \quad (7)$$

in which i is the cell current density, which is greater than or equal to i_{lim}.

Accordingly, the hydroxide ion transport number $t_{OH,AEL}$ is calculated as

$$t_{OH,AEL} = 1 - t_{Na,AEL} - t_{Cl,AEL} \quad (8)$$

Given that the bipolar membrane is modelled as symmetrical, the following equalities apply:

$$t_{Na,CEL} = t_{Cl,AEL} \quad (9)$$

$$t_{Cl,CEL} = t_{Na,AEL} \quad (10)$$

$$t_{H,CEL} = t_{OH,AEL} \quad (11)$$

The migrative flux of hydroxide ions through the CEL, as well as of proton ions through the AEL, are neglected, and thus their transport numbers as co-ions are null.

The following Donnan equilibrium is applied at each BPM layer (BPL) - solution interface:

$$\frac{R_gT}{z_{Na}F}ln\frac{C_{Na,sol,int}}{C_{Na,BPL,int}} = \frac{R_gT}{z_{Cl}F}ln\frac{C_{Cl,sol,int}}{C_{Cl,BPL,int}} \quad (12)$$

where $C_{i,sol,int}$ and $C_{i,BPL,int}$ are the ion concentrations at the solution-BPM interface on the channel (*ch*) or on the transition region (*tr*) side and BPM-layer side, respectively. R_g is the gas constant and T is the temperature.

The electro-neutrality within the BPM layers is considered with the general expression:

$$X_{BPL} + \sum C_{co,BPL} = \sum C_{ct,BPL} \quad (13)$$

where X_{BPL} is the fixed charge group concentration in the BPL, and $C_{co,BPL}$ and $C_{ct,BPL}$ are the co-ion and counter-ion concentrations in BPL phase.

Following the Strathmann's approach [27], within the salt transport region where current densities are lower than the limiting current density, it is assumed that the fixed charges are electrically balanced by the counter-ions in their respective layers. Therefore, at the membrane-solution interface on the interlayer side, the following assumptions are used

$$C_{Na,CEL,tr} = X_{BPL} \quad (14)$$

$$C_{Na,AEL,tr} = 0 \quad (15)$$

Once the limiting current condition has been reached, the sodium ion concentration will be zero. Therefore, i_{lim} is obtained by solving the set of equations shown above, with the following condition:

$$C_{Na,tr} = 0 \quad (16)$$

3.2. Middle-low scale: Triplet model

The triplet model regards the simulation of the repetitive units of the stack. This model was described in our previous work for the case of an acid-base flow battery [47] and is here adapted for BMED. It computes mass balances in each channel and provides the relevant electrical quantities such as the internal resistance, the boundary layer effect and the electro-motive force of the triplets.

The electric potential generated across each triplet is calculated according to the Nernst equation:

$$E = \sum_{IEMs}\left(-\frac{R_gT}{F}\int_{left,IEM}^{right,IEM}\sum_{ions}\frac{t^*_{i,IEM}}{z_i}dlna_{i,int}\right) \quad (17)$$

where $a_{i,int}$ is the activity of the i-th ion at the solution side of the membrane-solution interface (i.e., *right*, *IEM* and *left*, *IEM*, which are the right and left side of each membrane or membrane layer) and $t^{*}_{i,IEM}$ is the apparent ion transport number that are related to all the ions' diffusion coefficients and the average ion concentration inside the membrane.

The resistance of the triplet is calculated as the sum of a series of resistances:

$$R_{cell} = \sum_{sol} R_{sol} + \sum_{m} R_m \tag{18}$$

where R_{sol} is the electrical resistance (perpendicular to the membrane) of an electrolyte solution (i.e., acid, base or salt) and R_m is the electrical resistance of a membrane (i.e., CEM, AEM, or BPM). The model is numerically solved over a discretized spatial domain made up of 30 elements along the flow direction as for the channels model.

The main triplet model input are reported in Table 4.

The electrical resistance of the monopolar membranes was evaluated by model calibration by using the experimental data, starting from the manufacturer's information [51] as an initial approximation. The resistance of the bipolar membrane (not provided by the manufacturer) was estimated as the sum of the series of resistances of the CEL, AEL and interlayer [27] by assuming the resistivity of the layers equal to that of the corresponding monopolar membranes. The fixed charge density (FCD) was evaluated by dividing the Ion-Exchange Capacity (IEC) by the swelling degree (SD), and then multiplying by the water density. The IEC was given by the manufacturer for the monopolar membranes [51], but was not given for the BPM. For the three membrane types, the SD was not available from the manufacturer. Since this information was not available from other studies, SD values of Fumasep FKD and FKS membranes were employed [52] to estimate the FCD. The values of water permeability shown in Table 4 come from conventional electrodialysis membranes [53] because the values of this property were not known for the membranes used in the present study. Finally, the diffusivities in the membrane phase are tuning parameters of the model.

3.3. Middle-high scale: Stack model

This level includes the electrical sub-model for parasitic currents through the manifolds and the hydraulic sub-model. The former computes the distribution of the electric (ionic) currents through the stack, while the latter predicts pressure losses and flow distribution through the module.

Table 4
Main input of the triplet model.

Membrane properties						
		AEM	CEM	AEL	CEL	BPM
Thickness (d_m)	μm	130	130	95	95	190
Areal resistance* (R_m)	Ω cm^2	8.1	6.9	–	–	15
Water permeability (L_p)	ml bar^{-1}h^{-1} m^{-2}	8	8	–	–	–
H^+ diffusivity ($D_{H,m}$)	m^2 s^{-1}	1.4E-10	4.7E-11	2.0E-11	8.8E-11	–
Na^+ diffusivity ($D_{Na,m}$)	m^2 s^{-1}	4.7E-11	1.6E-11	1.6E-11	0.5E-11	–
Cl^- diffusivity ($D_{Cl,m}$)	m^2 s^{-1}	8.5E-11	2.8E-11	1.7E-11	0.6E-11	–
OH^- diffusivity ($D_{OH,m}$)	m^2 s^{-1}	9.4E-11	3.1E-11	2.4E-10	0.6E-11	–
Fixed charge density (X_m)	mol m^{-3}	5,000	5,000	5,000	5,000	–

* ~18% higher areal resistances were experimentally observed when sodium chloride was present in the acid and base channels. This variation was included in the model.

3.3.1. Electrical model

The equivalent electric circuit of the stack is shown in Fig. 5. The model calculates the electric current flowing through the cell resistances (R_k) perpendicular to the membranes, and the parasitic electric currents flowing through the longitudinal resistances ($R_{x,sol,k}$, x = up or down), and the manifolds ($R_{man,sol,k}$, *man* = distributor, *d*, or collector, *c*). i.e. collectors and distributors.

Once the resistances (depending on the conductivity of the solutions) have been calculated, Kirchhoff's law is applied to each node, and the first Ohm law is applied to each branch. Hence, electric currents through the branches and electric potential at the nodes are calculated.

The cell current for the *k*-th node I_k and the external current I_{ext} are calculated as:

$$I_k = \frac{(\Delta V_k - E_{av,k})}{R_{av,k}} \tag{19}$$

$$I_{ext} = \frac{U_{ext} - U}{R_{bl}} \tag{20}$$

where $E_{av,k}$ and ΔV_k are the average electromotive force (along the flow direction) and the total voltage drop, respectively, over the *k*-th triplet; R_{bl} and $R_{av,k}$ are the blank and the average cell resistance of the *k*-th triplet; U is the overall potential difference applied to the triplets and U_{ext} is the overall applied potential (including the blank voltage drop).

3.3.2. Hydraulic model

Fig. 6 reports a scheme of the hydraulic circuit simulated for one of the three solutions by the hydraulic sub-model at stack level. The circuit includes a distributor, a collector and the channel pathways of the electrolyte solution.

The distributed pressure losses within the channels were computed as:

$$\Delta P_{fd,sol} = f \rho_{sol} \frac{L}{4 d_{sol}} \left(u_{ch,sol}\right)^2 \tag{21}$$

where f is the Darcy friction factor evaluated by CFD correlations [47], ρ_{sol} is the mass density, L is the spacer length, and $u_{ch,sol}$ is the mean velocity of the solution (i.e., acid, base or salt) in the channel. The calculation of single pressure losses in the inlet/outlet part of the spacer-filled channel was carried out as

$$\Delta P_{l,sol} = k_{spacer} \frac{\rho_{sol}}{2} \left(u_{ch,sol}\right)^2 \tag{22}$$

where k_{spacer} is a local loss coefficient assessed by CFD correlations [47]. A similar equation was utilized to compute the pressure drop in the small tracts of manifolds between adjacent channels.

The total stack pressure loss was assessed through the sum of two addends: the pressure difference between the inlet and outlet of the manifolds and a further contribution due to the distribution/collection of the solution entering or exiting from the stack through the three inlet/outlet holes of the spacers mentioned in Section 2.

3.4. Highest scale: External hydraulic circuit

This model level takes into account the presence of the external hydraulic circuit (and eventually of auxiliary units) as well as the tanks for the storage of the electrolyte solutions. It calculates pressure drops in the external hydraulic circuits for acid, saline and alkaline solutions and, via mass balances with accumulation term, simulates the dynamic behavior of the BMED unit, for example during a closed-loop operation [47]. More precisely, once a time step has been chosen, the "new" concentration calculated by these transient mass balances (e.g., time = t_i) is used as a new input for the EDBM steady state model equations (those relevant to the other model scales) which (as output) provide an outlet concentration. The latter is used as "old" concentration in the tank

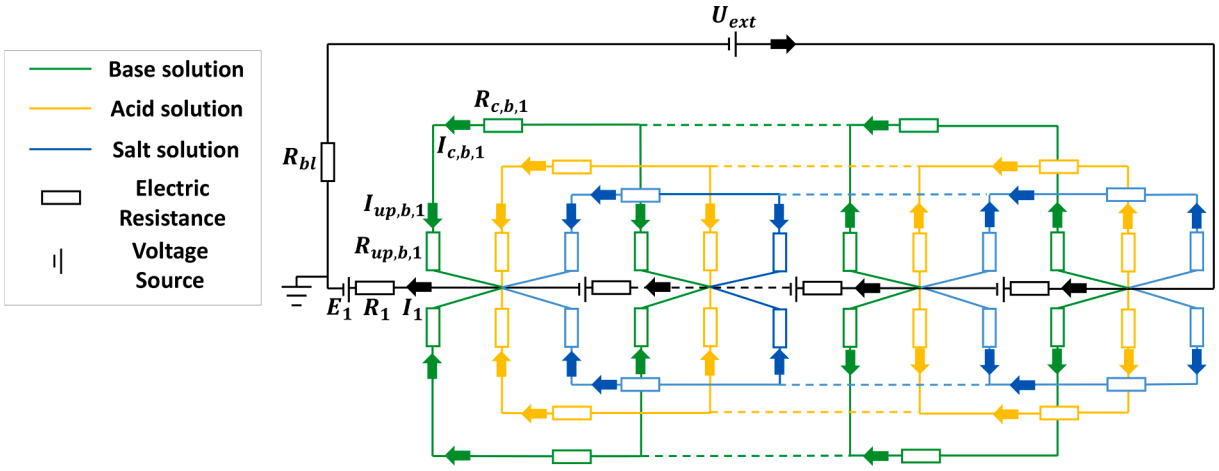

Fig. 5. Scheme of the equivalent electric circuit of BMED stacks.

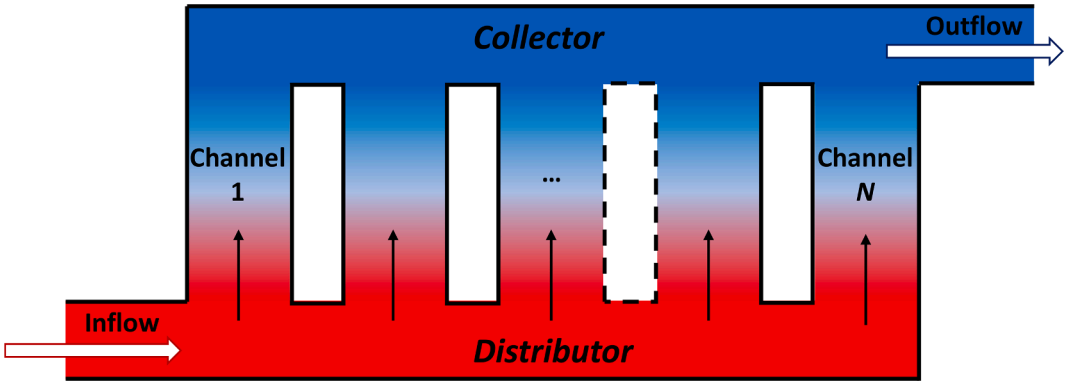

Fig. 6. Scheme of the hydraulic circuit for one of the three solutions: vertical ducts represent the channels, horizontal ducts represent the manifolds (distributor and collector) connecting the channels.

transient mass balances, thus generating again a "new" concentration (e.g., time = t_{i+1}) and closing the time step cycle. It is worth noting that this transient mass balances at the tanks do not make the multi-scale model fully dynamic as all the other model equations are written in a steady state regime. As a result, temporal interactions among processes are intrinsically not accounted for by the model which is unable to investigate the dynamics of any disturbance. These are not taken into account at the moment as the goal of the present paper is that of investigating the performance of EDBM units running continuously in a steady state mode in order to produce chemicals rather than trying to follow temporal variations due to disturbances.

3.5. Evaluation of the process performance

In this section, the main figures of merit used to characterize the performance of BMED processes are defined.

The current efficiency ($\eta_{c,OH}$) is the percentage of the total transported charge effectively converted in hydroxide ions:

$$\eta_{c,OH} = \frac{F\left(Q_{out,b}C_{OH,b,out} - Q_{in,b}C_{OH,b,in}\right)}{NI_{ext}} \tag{23}$$

where $C_{OH,b,out}$ and $C_{OH,b,in}$ are the hydroxyl ion concentrations in the base solution at the stack outlet and inlet, respectively, and $Q_{out,b}$ and $Q_{in,b}$ are the total flow rate of the base solution at the stack outlet and inlet, respectively.

The Specific Energy Consumption per unit mass (SEC_m) represents the kWh of energy consumed by the process to produce 1 kg of NaOH. It is given by [23]

$$SEC_m = \frac{U_{ext}I_{ext}}{3,600M_{NaOH}\left(Q_{out,b}C_{OH,b,out} - Q_{in,b}C_{OH,b,in}\right)} = \frac{U_{ext}}{3,600M_{NaOH}}\cdot\frac{F}{N\eta_c} \tag{24}$$

where M_{NaOH} is the molar mass of the sodium hydroxide.

The total or net Specific Energy Consumption of the process to produce 1 kg of NaOH ($SEC_{m,net}$) represents the total energy consumed by the process taking into account the energy spent for pumping:

$$SEC_{m,net} = \frac{U_{ext}I_{ext} + 3\ PPD\ L\ b\ N}{3,600M_{NaOH}\left(Q_{out,b}C_{OH,b,out} - Q_{in,b}C_{OH,b,in}\right)} \tag{25}$$

where *PPD* is the pumping power density calculated by the hydraulic model, *L* and *b* are the spacer length and width, and *N* is the number of repetitive units.

The *yield* of the sodium hydroxide (τ_{NaOH}) is the ratio between the molar flow rate of OH^- produced in the base compartments over the molar flow rate of sodium chloride at the inlet of the salt compartments

$$\tau_{NaOH} = \frac{\left(Q_{out,b}C_{OH,b,out} - Q_{in,b}C_{OH,b,in}\right)}{Q_{in,s}C_{Na,s,in}} \tag{26}$$

where $Q_{in,s}$ is the total inlet flow rate of the salt solution, and $C_{Na,s,in}$ is the sodium ion concentration at the inlet of the salt channel.

The specific yearly productivity of tons of NaOH per unit membrane area is defined as:

$$SP_{NaOH} = \frac{3.6 \bullet 8 M_{NaOH} \left(Q_{out,b} C_{OH,b,out} - Q_{in,b} C_{OH,b,in} \right)}{N\ 3\ L\ b} \quad (27)$$

The % parasitic loss of current (I_{loss}) is the fraction of the external current lost due to the shunt currents via the manifolds. It is given by

$$I_{loss} = \frac{I_{ext} - \frac{\sum_1^N I_k}{N}}{I_{ext}} \quad (28)$$

4. Results and discussions

4.1. Model validation and comparison with the state of the art

The model validation was firstly performed under once-through operation. Fig. 7 shows the polarization curves (i.e., voltage vs current curves) of the BMED process performed either without (graph (a)) or with (graph (b)) background salt in the acid and base solutions.

The experimental data showed high repeatability: a maximum percentage error of ~ 2.8% was found (see error bars in Fig. 7).

The model predictions were in good agreement with the experimental results for a wide range of current density, i.e. 20–250 A m^{-2}. Overall, the average discrepancy was lower than 3% for both sets of experiments (i.e., with and without the background salt).

Fig. 7 also reports the predictions of simplified versions of the model that neglect (i) shunt currents (dashed line), (ii) migrative transport of co-ions (dash-dotted line), (iii) or both phenomena (dotted line). Regardless of the presence of background salt, by not implementing the electrical model for parasitic currents, there was a significant overestimation (19.4% on average) of the external potential. As expected, the relative increase in external potential (to be applied to have the same current) was higher with higher number of triplets, reaching a maximum value of 31.3% in the case of a 38-triplet stack, without the presence of background salt. By not implementing the migrative transport of co-ions, there was an average increase of the external potential by 3.3%. Finally, when not including both the calculation of the parasitic currents and the migrative transport of co-ions, an average increase in the external potential of 23.5% is observed, with a maximum deviation of 35.2%.

A further comparison analysis between model predictions and experimental data was carried out in closed-loop configuration (i.e., dynamic operation). In order to evaluate the effectiveness of the present model, the simplified lumped model by Roux-de Balmann et al. [30] was also included into the comparison. It does not take into account the following aspects: diffusion of water and solutes, co-ion migration, shunt currents and concentration polarization. Fig. 8 shows the results in terms of NaOH and HCl concentrations in the base and acid tanks (assumed completely mixed), respectively, over the process time.

The concentrations were well-predicted by the present model, (average discrepancy of 2.1% and 1.0% and maximum discrepancy of 5.0% and 3.3% for the base and acid concentrations, respectively). For the simplified model, the average discrepancy was 14.6% and 13.9% for the base and acid concentrations, respectively, and the maximum one was ~ 24% regardless of the base and acid concentrations.

A reduction of the concentration increase rate was observed both experimentally and in the simulation with the present model. This is mainly due to non-ideal phenomena such as diffusion of solutes and transport of water. To a much lesser extent it is due to shunt currents, which are small in a stack with 5 triplets [43]. Indeed, the average % parasitic loss was calculated to be ~ 5%. Notably, the effects of non-ideal phenomena are amplified over time, thus resulting in large discrepancies between the simplified model and the experimental data. In the first minutes of the process, the curves of the two models are almost overlapped, while later on these curves depart from each other. This increasing disagreement over time should be considered somehow as also representative of what would occur over space in industrial scale

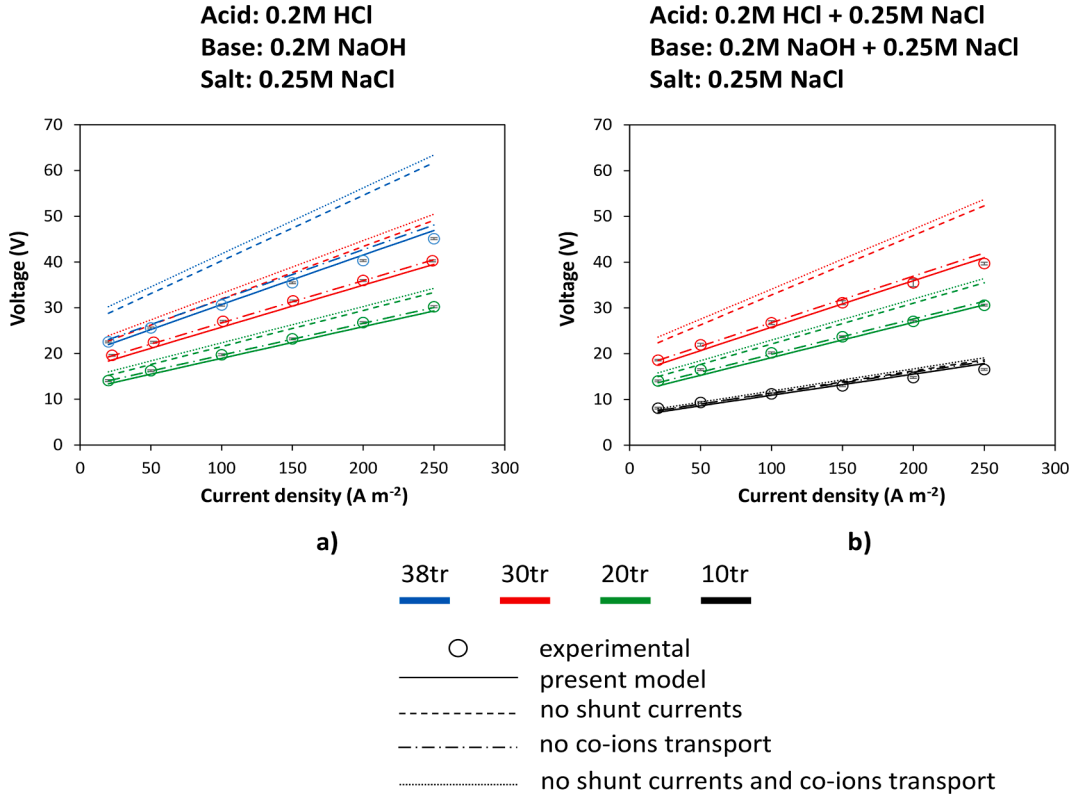

Fig. 7. Voltage–current density curves for stacks with different number of triplets: comparison between model predictions (lines) and experimental results (circles); (a) without the presence of background salt and (b) with the presence of background salt in the acid and base channels. Mean flow velocity of the solutions in each channel equal to 1 cm s^{-1}. Areal blank resistance: 72 Ω cm^2.

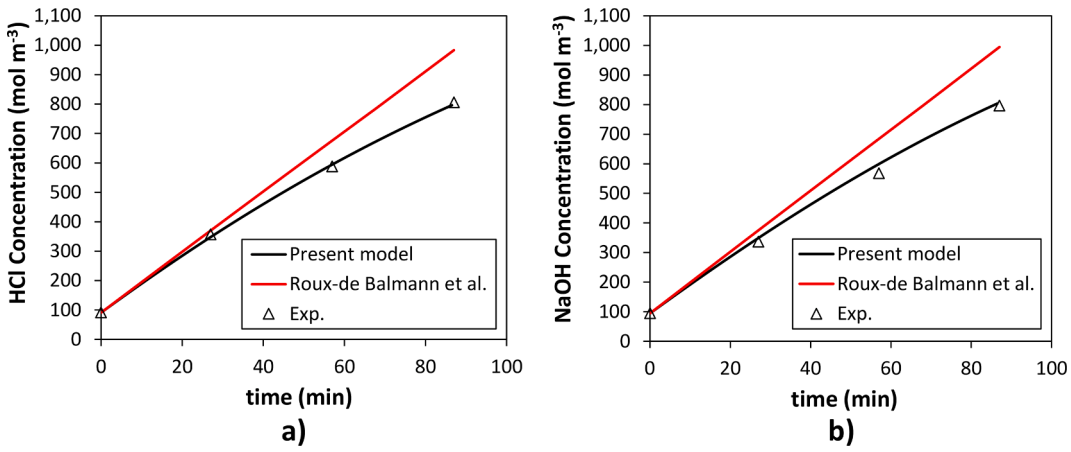

Fig. 8. Concentration vs time curves: comparison between model predictions (lines) and experimental results (triangle) for (a) hydrochloric acid and (b) sodium hydroxide in the acid and base channels, respectively. Mean flow velocity of the electrolyte solutions in each channel equal to 0.2 cm s^{-1}. Applied current density: 200 A m^{-2}. Areal blank resistance: 72 Ω cm^2. Number of triplets: 5. Additional details are reported in Table 3.

units working under once-through operation.

4.2. Multi-scale model capability

In order to demonstrate the greater predictive capability of the present model compared to existing ones, an industrial size BMED stack was simulated. In this case, the stack included 100 repetitive units with an active membrane area of 50 × 50 cm^2 in closed-loop mode. The applied current density was 100 A m^{-2}. Other settings had the values reported in Table 5.

The results are presented in terms of NaOH and HCl concentrations over time in Fig. 9.

Particularly, Fig. 9 also reports the predictions of simplified models that omit (i) shunt currents (dashed line), (ii) migrative transport of co-ions (dash-dotted line), (iii) or both phenomena (dotted line). Shunt currents had a greater impact on the simulation with 100 triplets, which had ~ 21% of I_{loss} at the final concentration. Therefore, the final concentration of acid and base predicted by the model without shunt currents deviated from the present complete model by ~ 13.5%. Co-ion transport affected the behavior of the EDBM unit even more. The final acid and base concentrations predicted by the simplified model neglecting co-ion transport was overestimated by ~ 24%. Neglecting both shunt currents and co-ion transport caused dramatic differences in the concentration profiles compared with those predicted by the complete model proposed in this study. In particular, the percentage differences were 47.7% and 40.3% for the final concentrations of HCl and NaOH, respectively. These results indicate that simplified models provide unsatisfactory predictions, thus being unreliable for the process characterization. Conversely, the proposed multi-scale model provides realistic and reliable predictions, thus being an effective tool that can be used not only for designing the unit, but also for guiding and optimizing the process.

Table 5
Operating conditions and starting concentrations for the industrial size closed-loop simulations. Areal blank resistance: 72 Ω cm^2.

N° triplets (N)	-	100
HCl concentration in the acid solution ($C_{a,HCl,in}$)	mol m^{-3}	50
Acid solution volume ($V_{a,in}$)	l	300
NaOH concentration in the base solution ($C_{b,NaOH,in}$)	mol m^{-3}	50
Base solution volume ($V_{b,in}$)	l	300
NaCl concentration in the salt solution ($C_{s,NaCl,in}$)	mol m^{-3}	2,000
Salt solution volume ($V_{s,in}$)	l	300
Mean flow velocity ($u_{ch,sol}$)	cm s^{-1}	1.0
Applied current density (i_{ext})	A m^{-2}	100

4.3. Simulations of industrial scale BMED units

In this section, the potential of the BMED for use at the industrial scale is assessed by a preliminary sensitivity analysis. The simulated process regards the BMED treatment of industrial brines with concentration within the interval of 0.5–2 M NaCl in once-through mode. The main input data are reported in Table 6.

Firstly, three case studies are considered by letting the active membrane area to vary, i.e. 0.75 × 0.75, 0.50 × 0.50 and 0.25 × 0.25 m^2, hereafter named as case A, B and C, respectively. For each case study, two sets of simulations were performed: the first concerns the sensitivity to the current density within the interval of 100–500 A m^{-2} at a fixed mean flow velocity of 1 cm s^{-1}; the second regards the sensitivity to the mean flow velocity within the interval of 0.5–5 cm s^{-1} at a fixed current density of 300 A m^{-2}. Both of these sets of simulations were performed at 1 M inlet NaCl concentration. Secondly, a set of simulations was performed for case study B to assess the sensitivity to the inlet salt concentration within the interval of 0.5–2 M NaCl (see section 4.3.3). In this case, the simulations were performed at fixed current density of 300 A m^{-2} and fixed mean flow velocity of 1 cm s^{-1}.

4.3.1. Sensitivity to current density

Fig. 10a shows the yield as a function of the applied current density for the three case studies.

The yield increases with the current density slightly less than linearly due to the presence of non-ideal phenomena, such as ion diffusion and water transport. The increase in yield from cases C to A is simply caused by an increase in the amount of moles transported per unit time across the membrane, whose area is larger. The yield clearly increases with greater applied current density as a result of the higher water dissociation rate for producing acid and base. Within the same current range, the average yield values obtained are 41, 27.3 and 12.6% for the three investigated scenarios A, B and C, respectively. Furthermore, as the active membrane area increases, the yield does not proportionally increase as would be expected. For example, if spacer length increases from 0.25 m to 0.75 m, the average yield should rise from 12.6% to 37.8%, thus tripling the value. However, the average yield of 41% in scenario A is higher than expected. This results from the effects of two contrasting phenomena. Firstly, ion diffusion and water transport (i.e., osmosis and electro-osmosis) increase with greater active membrane area. However, in the investigated scenarios, the spacer length tripled when passing from scenario C to scenario A. This leads to an increase in the longitudinal resistances $R_{x,sol,k}$ (see section 3.3.1), which causes a reduction in the I_{loss} from 15.7 to 2.7%, thus ultimately improving the yield.

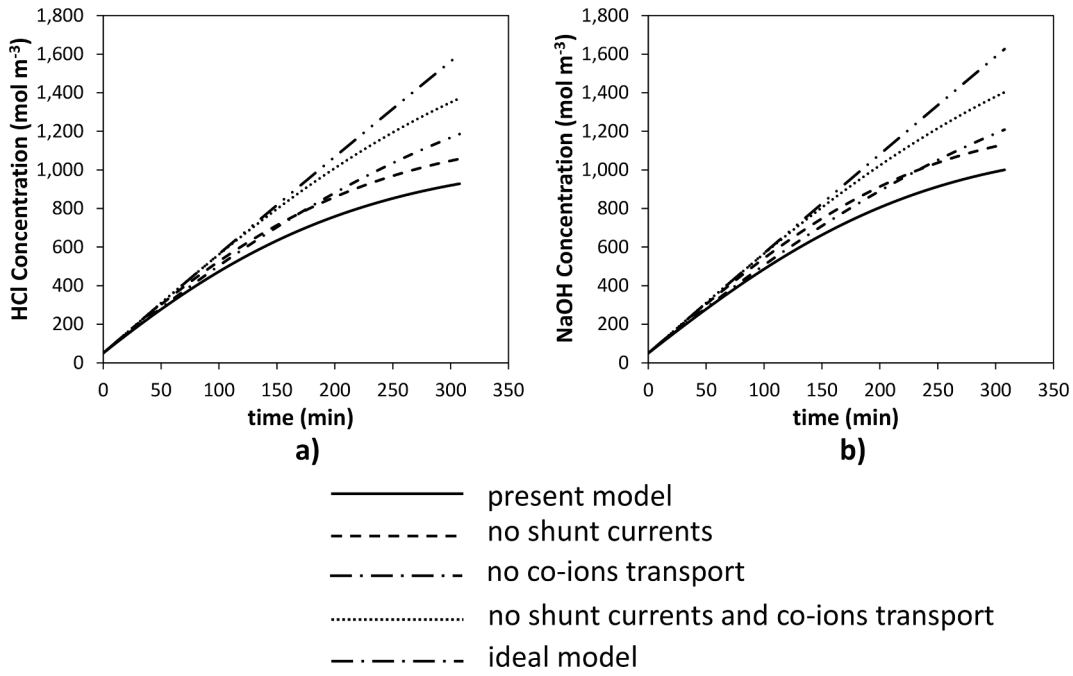

Fig. 9. Concentration vs time curves: comparison between model predictions for (a) hydrochloric acid and (b) sodium hydroxide in the acid and base channels, respectively. Mean flow velocity of the electrolyte solutions in each channel equal to 1.0 cm s^{-1}. Applied current density: 100 A m^{-2}. Areal blank resistance: 72 Ω cm^2. Number of triplets: 100. Additional details are reported in Table 5.

Table 6
Main model input of the industrial scale simulations.

Geometrical features				
		Scenario		
		A	B	C
Spacer length (L)	cm	75	50	25
Spacer width (b)	cm	75	50	25
Spacer thickness (d_m)	μm	475		
N° spacer holes (N_{holes})	–	3		
Spacer hole diameter (d_{man})	mm	8		
N° triplets (N)	–	100		
Process conditions				
HCl concentration in the acid solution ($C_{a,HCl,in}$)	mol m^{-3}	50		
NaOH concentration in the base solution ($C_{b,NaOH}$)	mol m^{-3}	50		
NaCl concentration in the salt solution ($C_{s,NaCl}$)	mol m^{-3}	500 – 2,000		
Mean flow velocity ($u_{ch,sol}$)	cm s^{-1}	0.5–5		
Applied current density (i_{ext})	A m^{-2}	100–500		
Blank resistance (R_{bl})	Ω cm^2	72		

Higher yields are associated to higher outlet concentrations. Fig. 10b shows that the maximum concentration is ~ 0.7 M, which corresponded to a yield just below ~ 70%. Therefore, this preliminary analysis shows that the use of feasible BMED designs (in terms of triplets number, membrane area) may allow the attainment of high NaOH yields in continuous once-through mode.

Fig. 11 shows the Specific Energy Consumption and current efficiency for the three case studies.

The SEC_m values range from a minimum of 0.68 kWh kg^{-1}_{NaOH} for case A at 100 A m^{-2}, to a maximum of 1.71 kWh kg^{-1}_{NaOH} for case C at 500 A m^{-2} (Fig. 11a). The increase in current density from 100 to 500 A m^{-2} causes an increase in SEC_m of ~ 2.4 times on average. Indeed, SEC_m is directly proportional to the ratio between the external potential and the current efficiency, as shown in Eq. (24). The latter shows a negligible increase when increasing the current density, thus the trend of SEC_m is mainly due to the U_{ext} variation. Particularly, U_{ext} is partly a function of the external current (according to the first Ohm law), and partly related to the electromotive force. The ohmic contribution increases almost linearly with the external current, thus becoming ~ 5 times greater when changing the current density from 100 to 500 A m^{-2}, whilst the electromotive force shows an increase of only ~ 17% across the same range of current. In absolute terms, the three case studies show similar performance when varying the applied current density, with an average SEC_m of 1.24 kWh kg^{-1}_{NaOH} (Fig. 11a). Indeed, the increase in membrane area leads to two contrasting effects. On the one hand, there is a higher effect of ion diffusion and transport of water. On the other hand, there is a reduction of shunt currents due to the higher longitudinal resistances $R_{x,sol,k}$ (see section 3.3.1).

A more detailed analysis can be made by plotting the energy consumption as a function of the yield. As shown in Fig. 11b, the case study A is again the best option when the yield is fixed. As a matter of fact, in this case with higher spacer length, the reduction in parasitic currents predominates over the increase in other detrimental phenomena [43].

The lower values of energy consumption for case study A are related to a higher current efficiency, as it can be seen in Fig. 11c. The average current efficiencies are 95.5, 92.7 and 82.3% for cases A, B and C respectively. Additionally, as the current density increases, the current efficiency increases. This is the result of both direct and indirect phenomena with counteracting effects. One of them is the electro-osmotic flux, which is enhanced by an increase in current density. Moreover, although the diffusion phenomenon is not directly related to the current density (as the driving force of diffusion is the concentration gradient of the species), it can be augmented by the resulting increase in the average concentration difference along the channels. On the other hand, the higher the current density, the lower the effect of parasitic currents. In particular, this effect is dominant over the increase in the non-ideal transport phenomena. However, especially in cases A and B, the high values of current efficiency suggest that co-ions transport is only marginal, and thus most of the carried current is being used to produce acid and base molecules.

4.3.2. *Sensitivity to mean channel flow velocity*

Fig. 12a shows the yield as a function of the mean flow velocity for the three case studies.

The average yield is found to be ~ 22.8, 15.1 and 6.94% for case

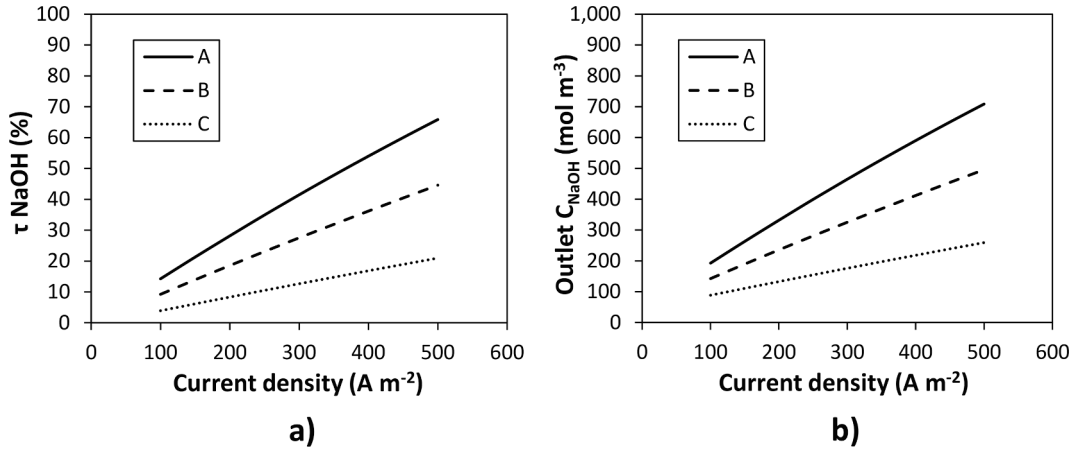

Fig. 10. a) Yield of sodium hydroxide and b) outlet sodium hydroxide concentration as functions of the current density for the three case studies (A, B and C) of active area (75 × 75, 50 × 50 and 25 × 25 cm^2) with a fixed mean channel flow velocity of 1 cm s^{-1}.

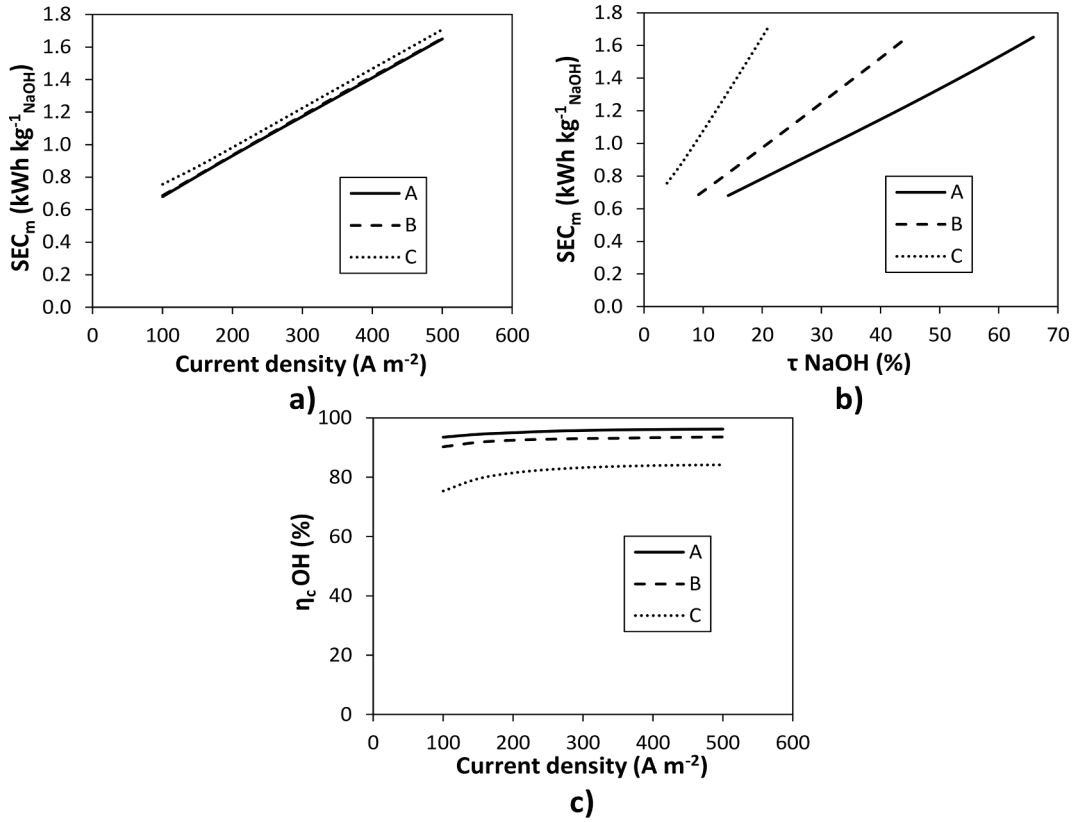

Fig. 11. Specific Energy Consumption per kilogram of produced NaOH as a function of a) the current density and b) the yield. c) Current efficiency as a function of the current density. The three graphs refer to the three cases (A, B and C) of active area (75 × 75, 50 × 50 and 25 × 25 cm^2), with a fixed mean channel flow velocity of 1 cm s^{-1}.

studies A, B and C respectively. As the mean flow velocities increases, the yield drastically decreases, with a tendency to flatten at high velocities. This trend is due to the reduction in the stream (i.e., along the channel) concentration change, which is taken accurately into account in the multi-scale model through the numerical discretization of the channel domain.

The SEC_m values (Fig. 12b) result in average values of 1.18 kWh kg^{-1}_{NaOH}. By increasing the mean flow velocity, the energy consumption decreases only slightly, due to the small effects of non-ideal transport phenomena. The trend in the current efficiency (Fig. 12c) as a function of the velocity is slightly decreasing because the current efficiency is inversely proportional to the SEC_m (see Eq. (24)). The current efficiency is not such a significant limitation for the three case studies; indeed, its average values are higher than 84%.

Fig. 12d shows the SEC_m as a function of the yield. The slight increment in SEC_m as the yield increases is due to the higher effect of non-ideal phenomena such as the parasitic currents and diffusion when the NaOH concentration difference between inlet and outlet increases. Cases A and B show similar performance, while scenario C has the worst performance because there is a visible increase in specific consumption with the same yield in NaOH. Similarly, to section 4.3.1, the greater the active membrane area, the lower the SEC_m. This is mainly due to the

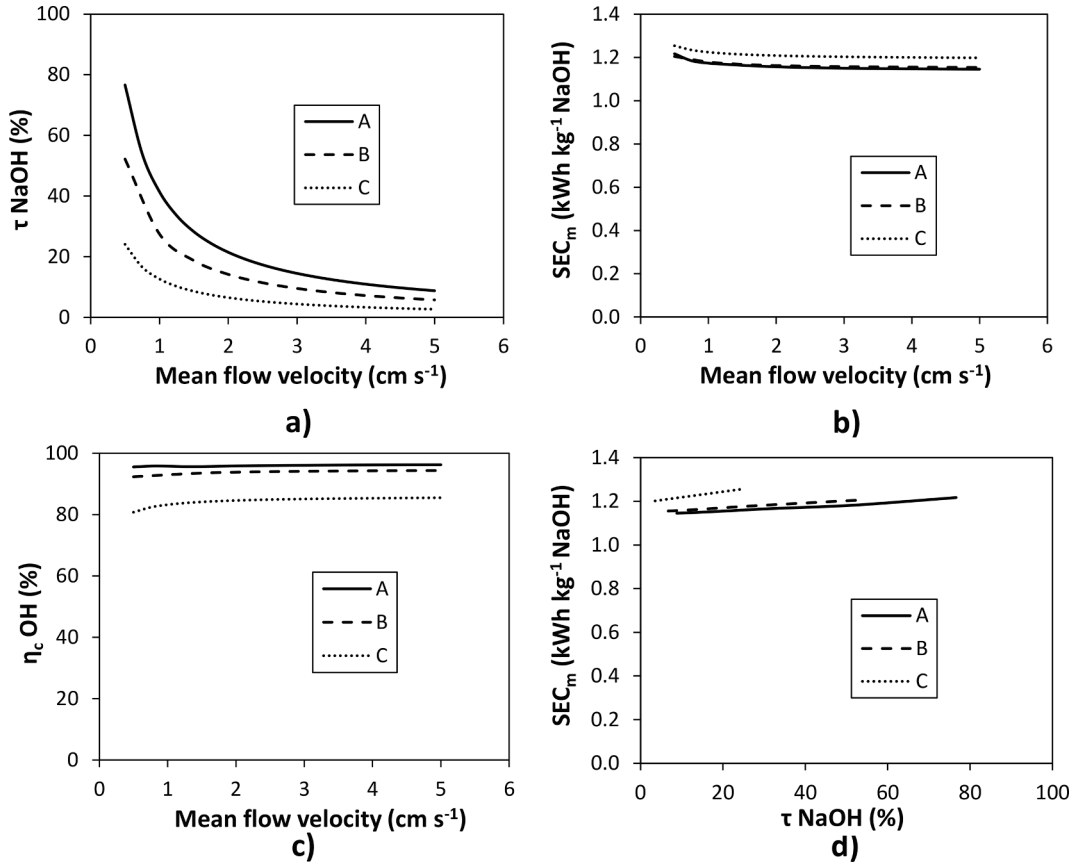

Fig. 12. a) Yield of sodium hydroxide, b) Specific Energy Consumption per kilogram of produced NaOH, c) Outlet sodium hydroxide concentration and d) Current efficiency as functions of the mean flow velocity for the three cases (A, B and C) of active area (75 × 75, 50 × 50 and 25 × 25 cm^2), with a fixed applied current density of 300 A m^{-2}.

increase of the longitudinal resistances ($R_{x,sol,k}$, x = up or down), which ultimately leads to a reduction in parasitic currents (I_{loss} from ~ 13.5% of scenario C to ~ 2% of scenario A).

Finally, Fig. 13 reports a comparison between net and gross Specific Energy Consumption.

The curves of the $SEC_{m,net}$ show trends with minimum values at 1.6, 2.3 and 1.6 cm s^{-1}, for cases A and B and C, respectively. As expected, this chart indicates that the difference between gross and net energy consumption increases as the mean flow velocity increases, as a result of the higher pressure drop. This result suggests that lower velocities may be beneficial to decrease the energy consumption, even though they lead to slightly lower current efficiencies.

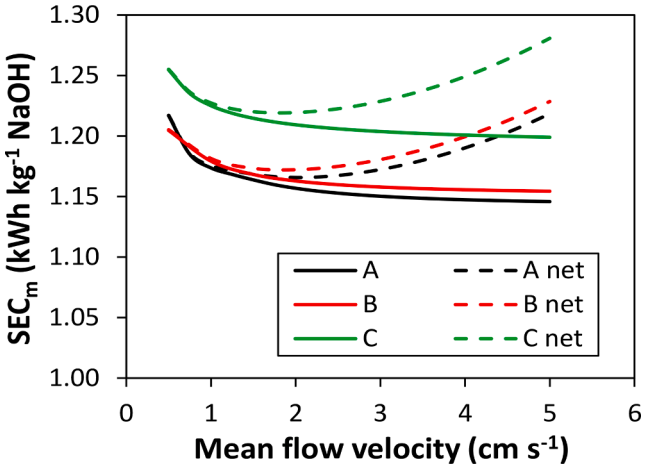

Fig. 13. Gross and Net Specific Energy Consumption per kilogram of produced NaOH as functions of the mean channel flow velocity for the three cases (A, B and C) of active area (75 × 75, 50 × 50 and 25 × 25 cm^2), with a fixed applied current density of 300 A m^{-2}. Continuous lines: SEC_m (gross). Dashed lines: net $SEC_{m,net}$.

4.3.3. *Sensitivity to inlet salt concentration*

In this section, the effect of varying the NaCl concentration in the salt compartment is investigated in two different scenarios, namely with or without background salt in the acid and base channels. Fig. 14a shows the Specific Energy Consumption per kg of produced NaOH as a function of the inlet NaCl concentration in the salt compartment for case study B, either without (black line) or with (red line) background salt (i.e., 0.25 M NaCl) in the acid and base channel feed solutions. The latter situation in which background salt is present may occur when waste saline solutions are used to feed the acid and base compartments. See (Fig. 15).

The results shown in Fig. 14 indicate that the performance of the EDBM stack is poorly dependent on the NaCl concentration in the saline compartment. In fact, regardless of the presence or absence of background salt in the acidic and alkaline solutions, both SEC_m and current efficiency only slightly decrease as the sodium chloride concentration in the saline feed is increased from 0.5 to 2 M. The slight decrease in SEC_m is caused by two different phenomena. On the one hand, current efficiency decreases slightly as the NaCl concentration in the salt compartment increases (Fig. 14b), implying an increase in the SEC_m (see Eq. (24)). On the other hand, the external electric potential (see Eq. (24)) decreases with the same increase in NaCl concentration due to reduced (i) electromotive force and (ii) cell resistance. These reductions prevail on the current efficiency increase, leading the SEC_m to decrease from 1.23 to 1.15 kWh kg^{-1}_{NaOH} in the absence of background salt and from

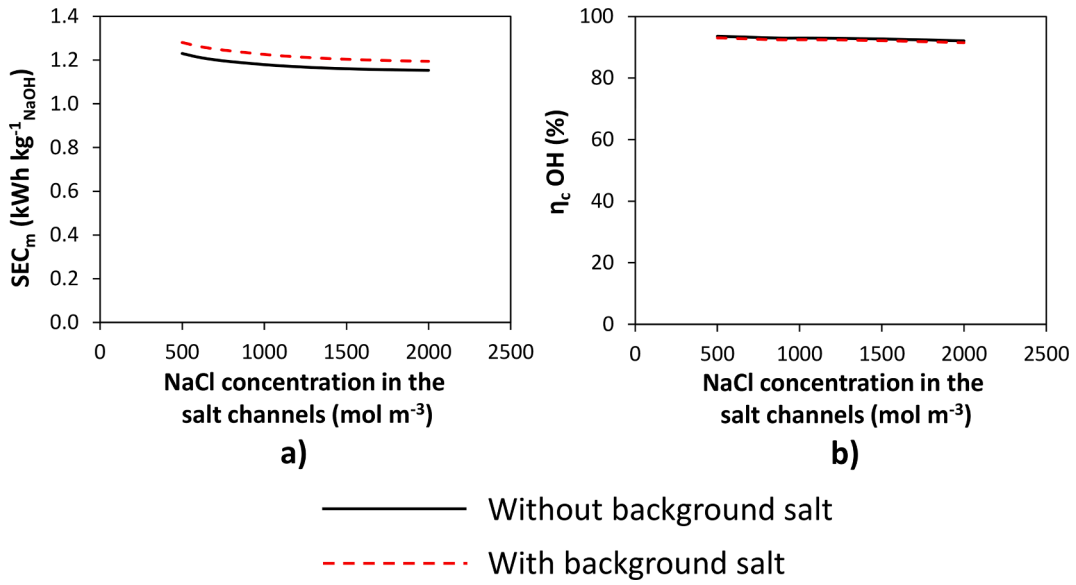

Fig. 14. a) Specific Energy Consumption per kilogram of produced NaOH and b) Current efficiency as functions of the inlet NaCl concentration in the salt compartment for the case B of active area (25 × 25 cm^2), with a fixed applied current density of 300 A m^{-2} and a fixed mean channel flow velocity of 1 cm s^{-1}. Black lines: without background salt in the acid and base channel feed solutions. Red lines: with 0.25 M NaCl in the acid and base channel feed solutions.

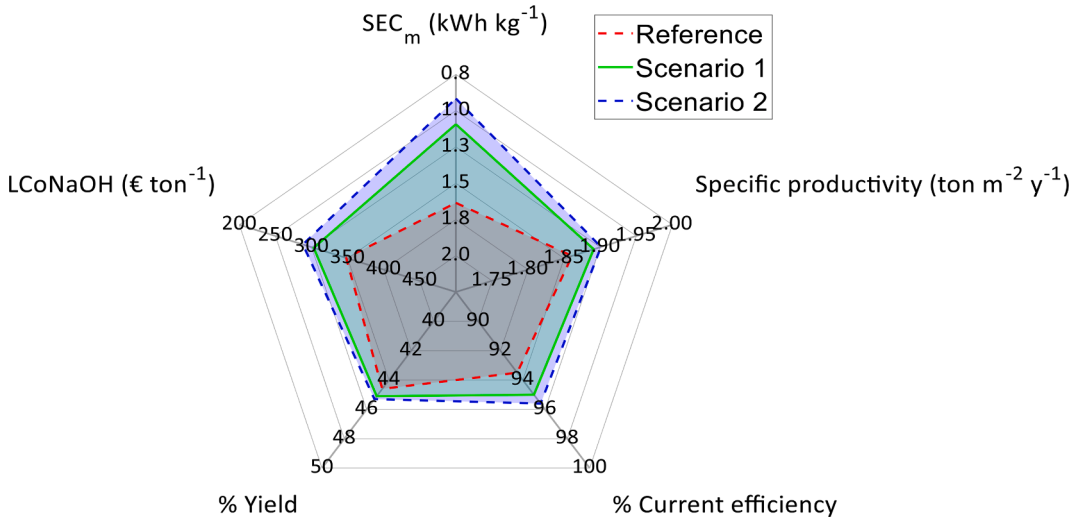

Fig. 15. Spider plot of Specific Energy Consumption per kg of produced NaOH, Specific productivity, % Current efficiency, % Yield, and Levelized Cost Of NaOH for the reference scenario and the scenarios 1 and 2 with enhanced membranes. Active area: 50 × 50 cm^2. Applied current density: 500 A m^{-2}. Mean flow velocity: 1 cm s^{-1}.

1.28 to 1.20 kWh kg^{-1}_{NaOH} in the presence of background salt.

Regarding the presence of background salt in the acid and base compartments, this has a small effect on SEC_m (i.e., slight increase), while it does not affect the current efficiency. Again, two counteracting factors contribute to the increase of SEC_m: the salt background leads the bipolar membrane potential to decrease and the membrane resistance to increase. The latter phenomenon is prominent, thus resulting in a 4% increase in the average SEC_m.

These results indicate that under the conditions here investigated, the saline compartment's concentration and the presence or absence of background salt in the acid and alkaline compartments has a small effect on the unit's performance. The small effect is clearly an outcome of the high selectivity of the Fumatech membranes adopted in this study. However, it is worth noting that the simulation results reported in Fig. 14 are relevant to once-through operational mode and a larger impact is expected in closed-loop applications when a fixed target of high acid/base concentration is requested.

4.3.4. *Sensitivity to the membrane properties: Preliminary techno-economic analysis*

In this section, a study on the effect of membrane properties is carried out. The results obtained when using standard membranes, as made for the sensitivity analysis discussed in sections 4.3.1, 4.3.2, and 4.3.3, are compared with two scenarios using enhanced membranes. The improvement in the membrane properties consists of reducing the electrical resistance, ionic diffusivities and water permeability. As shown in Table 7, these properties are halved in the scenario number 1, while they are reduced by three times in the scenario number 2. The reduction used in the enhanced scenarios should be regarded as optimistic yet still realistic, as similar values have been previously reported in the literature [52,54].

The study on the membrane properties is performed for case B of

Table 7
List of the improved membrane properties.

Improved membrane properties	Scenario 1	Scenario 2
Electrical resistance (R_m)	Current value (Table 4)/2	Current value (Table 4)/3
Ion diffusivities ($D_{i,m}$)	Current value (Table 4)/2	Current value (Table 4)/3
Water permeability (L_p)	Current value (Table 4)/2	Current value (Table 4)/3

active area (50×50 cm^{-2}) with an applied current density of 500 A m^{-2} and a mean flow velocity of 1 cm s^{-1}.

The different scenarios simulated for the membrane properties are used to perform a preliminary techno-economic analysis of the BMED process. The technical performance parameters considered are SEC_m, specific productivity, current efficiency, and yield. Additionally, the Levelized Cost Of Sodium Hydroxide (LCoNaOH), or Levelized Cost of Caustic Soda, is assessed to evaluate the potential economic competitiveness of the BMED technology. The LCoNaOH is the minimum sale price of 1 ton of sodium hydroxide required in order to obtain a Net Present Value (NPV) of zero at the end of the project lifetime:

$$LCoNaOH\left[\frac{€}{ton\ NaOH}\right] = \frac{Capitalcost + \sum_{y=1}^{n_{years}} \frac{O\&M_y + Cost\ \ Electricity_y}{(1+r)^y}}{\sum_{y=1}^{n_{years}} \frac{Mass_{NaOH,y}}{(1+r)^y}} \quad (29)$$

where *Capitalcost* is the initial total capital investment, $O\&M_y$ is the annual cost of operation, $CostElectricity_y$ is the cost of the electricity consumed by the BMED process, $Mass_{NaOH,y}$ is the mass of sodium hydroxide produced, y is the year, and r is the discount rate. The used economic parameters are reported in Table 8. Capital and maintenance costs are calculated according to Lei et al. [28]. The average 2021 Euro-to-dollar conversion rate of 1.18 was assumed.

The comparison between the standard and enhanced membranes is illustrated through the spider plot reported in Fig. 14, where each point represents a performance outcome of the techno-economic analysis. Each axis reports more desirable values from the center towards the vertices of the pentagon.

Table 8
Input parameters of the economic model.

Economic parameters			
Working hours	8,000 h y^{-1}		
Project lifetime	10 y		
Discount rate	5%		[55]
Electricity price	0.08 € kWh^{-1}	0.1 US$ kWh^{-1}	[28]
Capital costs			
AEM/CEM cost	114 € m^{-2}	135 US$ m^{-2}	[28]
BPM cost	1,140 € m^{-2}	1,350 US$ m^{-2}	[28]
Spacer cost	10 € m^{-2}	12 US$ m^{-2}	
Total cost of membranes and spacers	35,000 €	41,400 US$	
Cost of membrane stack	52,500 €	62,100 US$	1.5 × Total cost of membranes and spacer, [28]
Cost of peripherals	78,700 €	93,100 US$	1.5 × Cost of membrane stack, [28]
Total capital cost	131,200 €	155,100 US$	Cost of membrane stack + Cost of peripherals, [28]
Maintenance costs			
O&M cost	13,100 € y^{-1}	15,500 US$ y^{-1}	0.1 × Total capital cost, [28]

The SEC_m values are 1.7, 1.1 and 0.96 kWh kg$^{-1}_{NaOH}$ for the reference case, scenario 1, and scenario 2, respectively. The reduction of energy consumption is 31.4% and 41.8% in the improved membrane scenario 1 and 2, respectively. The lower diffusion coefficients together with the lower water permeabilities lead to a slightly better specific productivity of the produced caustic soda solutions, as it increases of 1.6% and 2.2%, when passing from the reference membranes to the scenario 1 and 2 membranes, respectively. Similarly, current efficiency (94.7% on average) and yield of caustic soda (45% on average) do not show significant differences when simulating improved membrane properties.

However, the lower values of energy consumption result in larger reductions of the LCoNaOH. Compared to the reference case, the LCoNaOH decreases of about 17% and 22.7% for the scenario 1 and 2, respectively. Specifically, the LCoNaOH drops to 288 € ton$^{-1}_{NaOH}$ (341 US$ ton$^{-1}_{NaOH}$) when the membrane properties are reduced by one third (scenario 2). Therefore, the use of improved membranes would lead to an important economic saving, provided that their own cost may be assumed to be unchanged compared to that of reference membranes. On the other hand, unlike other estimates reported in the literature [56,57], the LCoNaOH here evaluated also includes the effect of the discount rate.

Currently, the most common process for the production of NaOH is the chlor-alkali process. According to what has been reported in the literature, the price of caustic soda from chlor-alkali has been highly variable in recent years, with average values around 300 € ton$^{-1}_{NaOH}$ (355 US$ ton$^{-1}_{NaOH}$) [56], which is higher than the LCoNaOH calculated in this study. However, the output NaOH production from chlor-alkali has a higher concentration (around 10–30% by weight [57]) compared to that shown in this study (~2%). The outlet concentration of the BMED process may be increased by using a higher applied current density. However, this would lead to higher SEC_m values and, consequently, higher operating costs. An alternative process layout would be the coupling of the BMED unit with a caustic soda concentration unit, such as through vacuum evaporators with one or multiple effects. The benefits of the BMED process include the simultaneous production of an acid (i.e., HCl in this work), and of (at least partially) desalinated water. Moreover, BMED is a highly flexible technology as it can easily be adapted to the production of other bases and/or acids of commercial interest, e.g. for the production of potassium hydroxide starting from a potassium chloride feed solution.

5. Conclusions and future remarks

In this work, for the first time, a fully integrated BMED process model with distributed parameters was developed, following a multi-scale simulation strategy. Specifically, a configuration comprising three-chamber repetitive units was simulated. For the first time, a simulation tool was proposed to predict the effect of major non-ideal phenomena on the BMED operations.

The simulation tool was shown to be comprehensive and reliable through comparison with experimental data collected in steady-state and closed-loop configurations. The thoroughness of the present model enables the fully prediction of all the experimental data across varying operating conditions and number of triplets, thus confirming the predictive capability of the model for industrial scale simulations.

Additionally, a sensitivity analysis was carried out using this model simulating units with scaled-up dimensions in order to assess the potential performance for industrial applications. The results suggested that high yields of sodium hydroxide (about 70%) can be reached by increasing the applied current density to 500 A m^{-2} in stacks with 75 × 75 cm^2 of membrane area. Moreover, the higher the current density, the higher the resulting current efficiency. Similarly, higher current efficiencies may be reached when using greater active membrane area, due to the reduction of parasitic currents. Moreover, it was found that typical ranges of mean flow velocities (1–5 cm s^{-1}) do not significantly affect the module performance. Finally, a techno-economic analysis was

carried out, which assessed the cost of producing caustic soda from brines by means of a BMED unit. Specifically, the Levelized Cost Of Sodium Hydroxide (LCoNaOH) was evaluated across three different scenarios. In particular, this analysis demonstrated that the 50x50 cm^2 stacks provided with current membranes would lead to LCoNaOH of 348 € ton^{-1}_{NaOH} (411 US$ ton^{-1}_{NaOH}), while membranes with improved properties in terms of reducing the resistance, diffusivity, and water permeability by a factor of two or three, would lead to LCoNaOH of 303 € ton^{-1}_{NaOH} (358 US$ ton^{-1}_{NaOH}) or 288 € ton^{-1}_{NaOH} (340 US$ ton^{-1}_{NaOH}), respectively.

This techno-economic analysis was carried out with the aim of providing a first reliable assessment of the BMED competitiveness in relation to the currently used technology.

The developed innovative simulation tool can be utilized effectively for guiding the operations of BMED units, designing improved modules for the industrial scale, and enhancing their performance by identifying the optimal process conditions.

As future steps, in order to improve the sustainability of EDBM technology, industrial stacks are expected to be connected with renewable energy generation units which intrinsically operate in transient mode. Therefore, a further development of the multi-scale model making it fully dynamic will be mandatory to suitably track the fluctuating nature of these alternative energy sources. Finally, the present model could also be coupled with machine learning techniques [58] in order to predict complex and less deterministic phenomena such as membrane ageing and fouling.

Declaration of Competing Interest

The authors declare that they have no known competing financial interests or personal relationships that could have appeared to influence the work reported in this paper.

Acknowledgments

This work was performed in the framework of the BAoBaB project (*Blue Acid/Base Battery: Storage and recovery of renewable electrical energy by reversible salt water dissociation*). The BAoBaB project has received funding from the European Union's Horizon 2020 Research and Innovation program under Grant Agreement no. 731187 (http://www.baobabproject.eu).

References

[1] C. Huang, T. Xu, Electrodialysis with bipolar membranes for sustainable development, Environ. Sci. Technol. 40 (17) (2006) 5233–5243, https://doi.org/10.1021/es060039p.
[2] T. Xu, Electrodialysis processes with bipolar membranes (EDBM) in environmental protection—a review, Resour. Conserv. Recycl. 37 (1) (2002) 1–22, https://doi.org/10.1016/S0921-3449(02)00032-0.
[3] L. Gurreri, A. Tamburini, A. Cipollina, G. Micale, Electrodialysis applications in wastewater treatment for environmental protection and resources recovery: a systematic review on progress and perspectives, Membranes (Basel). 10 (2020) 146, https://doi.org/10.3390/membranes10070146.
[4] J. Xia, G. Eigenberger, H. Strathmann, U. Nieken, Flow battery based on reverse electrodialysis with bipolar membranes: Single cell experiments, J. Memb. Sci. 565 (2018) 157–168, https://doi.org/10.1016/j.memsci.2018.07.073.
[5] W.J. van Egmond, M. Saakes, I. Noor, S. Porada, C.J.N. Buisman, H.V.M. Hamelers, Performance of an environmentally benign acid base flow battery at high energy density, Int. J. Energy Res. 42 (4) (2018) 1524–1535, https://doi.org/10.1002/er.3941.
[6] H. Luo, X. Cheng, G. Liu, Y. Zhou, Y. Lu, R. Zhang, X. Li, W. Teng, Citric acid production using a biological electrodialysis with bipolar membrane, J. Memb. Sci. 523 (2017) 122–128, https://doi.org/10.1016/j.memsci.2016.09.063.
[7] N. van Linden, G.L. Bandinu, D.A. Vermaas, H. Spanjers, J.B. van Lier, Bipolar membrane electrodialysis for energetically competitive ammonium removal and dissolved ammonia production, J. Clean. Prod. 259 (2020), 120788, https://doi.org/10.1016/j.jclepro.2020.120788.
[8] W. Tian, X. Wang, C. Fan, Z. Cui, Optimal treatment of hypersaline industrial wastewater via bipolar membrane electrodialysis, ACS Sustain. Chem. Eng. 7 (2019) 12358–12368, https://doi.org/10.1021/acssuschemeng.9b01778.
[9] X. Sun, H. Lu, J. Wang, Recovery of citric acid from fermented liquid by bipolar membrane electrodialysis, J. Clean. Prod. 143 (2017) 250–256, https://doi.org/10.1016/j.jclepro.2016.12.118.
[10] J.S.J. Ferrer, S. Laborie, G. Durand, M. Rakib, Formic acid regeneration by electromembrane processes, J. Memb. Sci. 280 (1-2) (2006) 509–516, https://doi.org/10.1016/j.memsci.2006.02.012.
[11] P. Pinacci, M. Radaelli, Recovery of citric acid from fermentation broths by electrodialysis with bipolar membranes, Desalination 148 (1-3) (2002) 177–179, https://doi.org/10.1016/S0011-9164(02)00674-4.
[12] V. Kravtsov, I. Kulikova, S. Mikhaylin, L. Bazinet, Alkalinization of acid whey by means of electrodialysis with bipolar membranes and analysis of induced membrane fouling, J. Food Eng. 277 (2020) 109891, https://doi.org/10.1016/j.jfoodeng.2019.109891.
[13] A. Merkel, A.M. Ashrafi, J. Ečer, Bipolar membrane electrodialysis assisted pH correction of milk whey, J. Memb. Sci. 555 (2018) 185–196, https://doi.org/10.1016/j.memsci.2018.03.035.
[14] V.A. Kravtsov, I.K. Kulikova, A.S. Bessonov, I.A. Evdokimov, Feasibility of using electrodialysis with bipolar membranes to deacidify acid whey, Int. J. Dairy Technol. 73 (1) (2020) 261–269, https://doi.org/10.1111/1471-0307.12637.
[15] G. Dufton, S. Mikhaylin, S. Gaaloul, L. Bazinet, How electrodialysis configuration influences acid whey deacidification and membrane scaling, J. Dairy Sci. 101 (9) (2018) 7833–7850, https://doi.org/10.3168/jds.2018-14639.
[16] C. Aspirault, A. Doyen, L. Bazinet, Impact of Preheating Temperature on the Separation of Whey Proteins When Combined with Chemical or Bipolar Membrane Electrochemical Acidification, Int. J. Mol. Sci. 21 (2020) 2792, https://doi.org/10.3390/ijms21082792.
[17] S. Bunani, K. Yoshizuka, S. Nishihama, M. Arda, N. Kabay, Application of bipolar membrane electrodialysis (BMED) for simultaneous separation and recovery of boron and lithium from aqueous solutions, Desalination 424 (2017) 37–44, https://doi.org/10.1016/j.desal.2017.09.029.
[18] D. İpekçi, N. Kabay, S. Bunani, E. Altıok, M. Arda, K. Yoshizuka, S. Nishihama, Application of heterogeneous ion exchange membranes for simultaneous separation and recovery of lithium and boron from aqueous solution with bipolar membrane electrodialysis (EDBM), Desalination 479 (2020) 114313, https://doi.org/10.1016/j.desal.2020.114313.
[19] S. Bunani, M. Arda, N. Kabay, K. Yoshizuka, S. Nishihama, Effect of process conditions on recovery of lithium and boron from water using bipolar membrane electrodialysis (BMED), Desalination 416 (2017) 10–15, https://doi.org/10.1016/j.desal.2017.04.017.
[20] K. Ghyselbrecht, A. Silva, B. Van der Bruggen, K. Boussu, B. Meesschaert, L. Pinoy, Desalination feasibility study of an industrial NaCl stream by bipolar membrane electrodialysis, J. Environ. Manage. 140 (2014) 69–75, https://doi.org/10.1016/j.jenvman.2014.03.009.
[21] M. Herrero-Gonzalez, N. Admon, A. Dominguez-Ramos, R. Ibañez, A. Wolfson, A. Irabien, Environmental sustainability assessment of seawater reverse osmosis brine valorization by means of electrodialysis with bipolar membranes, Environ. Sci. Pollut. Res. 27 (2) (2020) 1256–1266, https://doi.org/10.1007/s11356-019-04788-w.
[22] C. Fernandez-Gonzalez, A. Dominguez-Ramos, R. Ibañez, A. Irabien, Electrodialysis with Bipolar Membranes for Valorization of Brines, Sep. Purif. Rev. 45 (4) (2016) 275–287, https://doi.org/10.1080/15422119.2015.1128951.
[23] M. Herrero-Gonzalez, P. Díaz-Guridi, A. Dominguez-Ramos, A. Irabien, R. Ibañez, Highly concentrated HCl and NaOH from brines using electrodialysis with bipolar membranes, Sep. Purif. Technol. 242 (2020) 116785, https://doi.org/10.1016/j.seppur.2020.116785.
[24] T. Tong, M. Elimelech, The Global Rise of Zero Liquid Discharge for Wastewater Management: Drivers, Technologies, and Future Directions, Environ. Sci. Technol. 50 (13) (2016) 6846–6855, https://doi.org/10.1021/acs.est.6b01000.
[25] Muhammad Yaqub, W. Lee, Lee, Zero-liquid discharge (ZLD) technology for resource recovery from wastewater: A review, Sci. Total Environ. 681 (2019) 551–563, https://doi.org/10.1016/j.scitotenv.2019.05.062.
[26] M. Mier, R. Ibanez, I. Ortiz, Influence of ion concentration on the kinetics of electrodialysis with bipolar membranes, Sep. Purif. Technol. 59 (2) (2008) 197–205, https://doi.org/10.1016/j.seppur.2007.06.015.
[27] H. Strathmann, J.J. Krol, H.-J. Rapp, G. Eigenberger, Limiting current density and water dissociation in bipolar membranes, J. Memb. Sci. 125 (1) (1997) 123–142, https://doi.org/10.1016/S0376-7388(96)00185-8.
[28] C. Lei, Z. Li, Q.i. Gao, R. Fu, W. Wang, Q. Li, Z. Liu, Comparative study on the production of gluconic acid by electrodialysis and bipolar membrane electrodialysis: Effects of cell configurations, J. Memb. Sci. 608 (2020) 118192, https://doi.org/10.1016/j.memsci.2020.118192.
[29] M. Szczygieła, K. Prochaska, Alpha-ketoglutaric acid production using electrodialysis with bipolar membrane, J. Memb. Sci. 536 (2017) 37–43, https://doi.org/10.1016/j.memsci.2017.04.059.
[30] H. Roux-de Balmann, M. Bailly, F. Lutin, P. Aimar, Modelling of the conversion of weak organic acids by bipolar membrane electrodialysis, Desalination 149 (1-3) (2002) 399–404, https://doi.org/10.1016/S0011-9164(02)00863-9.
[31] S. Koter, A. Warszawski, A new model for characterization of bipolar membrane electrodialysis of brine, Desalination 198 (1-3) (2006) 111–123, https://doi.org/10.1016/j.desal.2006.09.016.
[32] J.L. Gineste, G. Pourcelly, Y. Lorrain, F. Persin, C. Gavach, Analysis of factors limiting the use of bipolar membranes: A simplified model to determine trends, J. Memb. Sci. 112 (2) (1996) 199–208, https://doi.org/10.1016/0376-7388(95)00284-7.
[33] A. Ortega, L.F. Arenas, J.J.H. Pijpers, D.L. Vicencio, J.C. Martínez, F.A. Rodríguez, E.P. Rivero, Modelling water dissociation, acid-base neutralization and ion

transport in bipolar membranes for acid-base flow batteries, J. Memb. Sci. 641 (2022) 119899, https://doi.org/10.1016/j.memsci.2021.119899.
[34] C. Jiang, S. Li, D. Zhang, Z. Yang, D. Yu, X. Chen, Y. Wang, T. Xu, Mathematical modelling and experimental investigation of CO2 absorber recovery using an electro-acidification method, Chem. Eng. J. 360 (2019) 654–664, https://doi.org/10.1016/j.cej.2018.12.006.
[35] E. Vera, J. Sandeaux, F. Persin, G. Pourcelly, M. Dornier, J. Ruales, Modeling of clarified tropical fruit juice deacidification by electrodialysis, J. Memb. Sci. 326 (2) (2009) 472–483, https://doi.org/10.1016/j.memsci.2008.10.034.
[36] Y. Wang, A. Wang, X.u. Zhang, T. Xu, Simulation of Electrodialysis with Bipolar Membranes: Estimation of Process Performance and Energy Consumption, Ind. Eng. Chem. Res. 50 (24) (2011) 13911–13921, https://doi.org/10.1021/ie200467s.
[37] S.S. Melnikov, O.A. Mugtamov, V.I. Zabolotsky, Study of electrodialysis concentration process of inorganic acids and salts for the two-stage conversion of salts into acids utilizing bipolar electrodialysis, Sep. Purif. Technol. 235 (2020) 116198, https://doi.org/10.1016/j.seppur.2019.116198.
[38] S. Koter, Modeling of weak acid production by the EDB method, Sep. Purif. Technol. 57 (3) (2007) 406–412, https://doi.org/10.1016/j.seppur.2006.03.005.
[39] L. Gurreri, A. Filingeri, M. Ciofalo, A. Cipollina, M. Tedesco, A. Tamburini, G. Micale, Electrodialysis with asymmetrically profiled membranes: Influence of profiles geometry on desalination performance and limiting current phenomena, Desalination 506 (2021) 115001, https://doi.org/10.1016/j.desal.2021.115001.
[40] M. La Cerva, L. Gurreri, M. Tedesco, A. Cipollina, M. Ciofalo, A. Tamburini, G. Micale, Determination of limiting current density and current efficiency in electrodialysis units, Desalination 445 (2018) 138–148, https://doi.org/10.1016/j.desal.2018.07.028.
[41] L. Shi, Y. Hu, S. Xie, G. Wu, Z. Hu, X. Zhan, Recovery of nutrients and volatile fatty acids from pig manure hydrolysate using two-stage bipolar membrane electrodialysis, Chem. Eng. J. 334 (2018) 134–142, https://doi.org/10.1016/j.cej.2017.10.010.
[42] J. Veerman, J.W. Post, M. Saakes, S.J. Metz, G.J. Harmsen, Reducing power losses caused by ionic shortcut currents in reverse electrodialysis stacks by a validated model, J. Memb. Sci. 310 (1-2) (2008) 418–430, https://doi.org/10.1016/j.memsci.2007.11.032.
[43] A. Culcasi, L. Gurreri, A. Zaffora, A. Cosenza, A. Tamburini, A. Cipollina, G. Micale, Ionic shortcut currents via manifolds in reverse electrodialysis stacks, Desalination 485 (2020) 114450, https://doi.org/10.1016/j.desal.2020.114450.
[44] M. Tedesco, A. Cipollina, A. Tamburini, I.D.L. Bogle, G. Micale, A simulation tool for analysis and design of reverse electrodialysis using concentrated brines, Chem. Eng. Res. Des. 93 (2015) 441–456, https://doi.org/10.1016/j.cherd.2014.05.009.
[45] R.S. Jupudi, G. Zappi, R. Bourgeois, Prediction of shunt currents in a bipolar electrolyzer stack by difference calculus, J. Appl. Electrochem. 37 (8) (2007) 921–931, https://doi.org/10.1007/s10800-007-9330-4.
[46] Z. Peng, Y. Sun, Leakage circuit characteristics of a bipolar membrane electrodialyzer with 5 BP-A-C units, J. Memb. Sci. 597 (2020) 117762, https://doi.org/10.1016/j.memsci.2019.117762.
[47] A. Culcasi, L. Gurreri, A. Zaffora, A. Cosenza, A. Tamburini, G. Micale, On the modelling of an Acid/Base Flow Battery: An innovative electrical energy storage device based on pH and salinity gradients, Appl. Energy. 277 (2020) 115576, https://doi.org/10.1016/j.apenergy.2020.115576.
[48] M. Laliberté, W.E. Cooper, Model for calculating the density of aqueous electrolyte solutinos, J. Chem. Eng. Data. 49 (2004) 1141–1151, https://doi.org/10.1021/je0498659.
[49] K.S. Pitzer, J.J. Kim, Thermodynamics of Electrolytes, IV. Activity and Osmotic Coefficients for Mixed Electrolytes 96 (18) (1974) 5701–5707, https://doi.org/10.1021/ja00825a004.
[50] K.S. Pitzer, G. Mayorga, Thermodynamics of electrolytes. II. Activity and osmotic coefficients for strong electrolytes with one or both ions univalent, J. Phys. Chem. 77 (19) (1973) 2300–2308, https://doi.org/10.1021/j100638a009.
[51] Fumatech Bwt GmbH, Brochure on Ion Exchange Membranes, (n.d.). https://www.fumatech.com/NR/rdonlyres/3DF915E1-47B5-4F43-B18A-D23F9CD9FC9D/0/FUMATECH_BWT_GmbHIon_Exchange_Membranes.pdf.
[52] Y. Mei, C.Y. Tang, Recent developments and future perspectives of reverse electrodialysis technology: A review, Desalination 425 (2018) 156–174, https://doi.org/10.1016/j.desal.2017.10.021.
[53] M. La Cerva, L. Gurreri, A. Cipollina, A. Tamburini, M. Ciofalo, G. Micale, Modelling and cost analysis of hybrid systems for seawater desalination: Electromembrane pre-treatments for Reverse Osmosis, Desalination 467 (2019) 175–195, https://doi.org/10.1016/j.desal.2019.06.010.
[54] M. Micari, A. Cipollina, F. Giacalone, G. Kosmadakis, M. Papapetrou, G. Zaragoza, G. Micale, A. Tamburini, Towards the first proof of the concept of a Reverse ElectroDialysis - Membrane Distillation Heat Engine, Desalination 453 (2019) 77–88, https://doi.org/10.1016/j.desal.2018.11.022.
[55] F. Giacalone, M. Papapetrou, G. Kosmadakis, A. Tamburini, G. Micale, A. Cipollina, Application of reverse electrodialysis to site-specific types of saline solutions: A techno-economic assessment, Energy. 181 (2019) 532–547, https://doi.org/10.1016/j.energy.2019.05.161.
[56] P. Arora, V. Srinivasan, Report on the Electrolytic Industries for the Year 2001, J. Electrochem. Soc. 149 (11) (2002) K1, https://doi.org/10.1149/1.1514962.
[57] T. Brinkmann, G. Giner Santonja, F. Schorcht, S. Roudier, L. Delgado Sancho, Best Available Techniques Reference Document for the Production of Chlor-alkali, 2014. https://doi.org/10.2791/13138.
[58] Y. Wang, B. Seo, B. Wang, N. Zamel, K. Jiao, X.C. Adroher, Fundamentals, materials, and machine learning of polymer electrolyte membrane fuel cell technology, Energy AI. 1 (2020) 100014, https://doi.org/10.1016/j.egyai.2020.100014.